

# The Deep Eutectic Solvent Precipitation Synthesis of Metastable $\text{Zn}_4\text{V}_2\text{O}_9$

Sangki Hong,<sup>1</sup> Ye Cheng,<sup>2</sup> Shruti Hariyani,<sup>3</sup> Jingzhe Li,<sup>1,4</sup> Rachel M. Doughty,<sup>2</sup> Aishwarya Mantravadi,<sup>1</sup> Emily A. Smith,<sup>1,4</sup> Jakoah Brgoch,<sup>3</sup> Frank E. Osterloh,<sup>2</sup> Julia V. Zaikina<sup>1\*</sup>

<sup>1</sup> *Department of Chemistry, Iowa State University, Ames, Iowa 50011, United States*

<sup>2</sup> *Department of Chemistry, University of California at Davis, Davis, California 95616, United States*

<sup>3</sup> *Department of Chemistry, University of Houston, Houston, Texas 77004, United States*

<sup>4</sup> *U.S. Department of Energy, Ames Laboratory, Ames, Iowa 50011, United States*

**Abstract.** A precipitation method involving a deep eutectic solvent (DES) — a mixture of hydrogen bond donor and acceptor — is used for the synthesis of ternary metal oxide. Without toxic reagents, precipitates consisting of  $\text{Zn}_3(\text{OH})_2\text{V}_2\text{O}_7 \cdot n\text{H}_2\text{O}$  and  $\text{Zn}_5(\text{OH})_6(\text{CO}_3)_2$  are obtained by simply introducing deionized (DI)  $\text{H}_2\text{O}$  to the DES solution containing dissolved  $\text{ZnO}$  and  $\text{V}_2\text{O}_5$ . Manipulation of the synthetic conditions demonstrates high-tunability in size/morphology of the two-dimensional nanosheets precipitated during the dynamic equilibrium process. According to the differential scanning calorimetry and high-temperature powder X-ray diffraction,  $\text{Zn}_3\text{V}_2\text{O}_8$  and  $\text{ZnO}$  intermediates obtained from the zinc dihydroxide divanadate hydrate and zinc carbonate hydroxide, respectively, are utilized in the reaction pathway toward metastable  $\text{Zn}_4\text{V}_2\text{O}_9$ . Intimate mixing of the metal precursors achieved by the precipitation method allows to access the metastable zinc-rich vanadate with an unusually rapid heat treatment. Four nonequivalent vanadium sites within  $\text{Zn}_4\text{V}_2\text{O}_9$  cause the splitting of the  $[\text{VO}_4]^{3-}$  vibrational mode in the corresponding Raman spectrum. The optical band gap of the zinc vanadate is found to be 2.94 eV, significantly smaller ( $\sim 1.0$  eV) than the DFT-calculated value. Both UV-vis and surface photovoltage spectra reveal the presence of sub-band gap states, stemming from the reduced vanadium ( $\text{V}^{4+}$ ) center. The defect diminishes electron charge transfer from O  $2p$  orbital to vacant  $3d$  orbital of  $\text{V}^{5+}$  in  $\text{VO}_4$  tetrahedra upon photoexcitation. Photoelectrochemical measurements confirm weak photoanodic currents for water and methanol oxidation. This work shows, for the first time, the synthesis of a metastable oxide with the DES-precipitation route and provides insight into a structure-property relationship of the zinc-rich vanadate.

## Introduction

Metastable materials, which lie at the local minima of energy landscape, expand our understanding of structure and property relationship. Density functional theory (DFT) together with large material databases such as Open Quantum Materials Database (OQMD)<sup>1</sup> and Inorganic Crystal Structure Database (ICSD)<sup>2,3</sup> allow for high-throughput discovery of new metastable compounds above convex hull of chemical space.<sup>4</sup> However, computational predictions have gone beyond experimental synthetic ability. Although identification of thermodynamic upper limit in the energy scale helps determine which materials are synthesizable or not,<sup>5,6</sup> evaluation of various synthetic parameters towards synthesizability is currently unavailable in computational methods. Conspicuous efforts with variety of synthetic techniques have been made to access metastable materials. For instance, high-pressure synthesis was utilized to prepare multiferroic BiMnO<sub>3</sub>.<sup>7</sup> A potential solar cell absorber  $\beta$ -CuGaO<sub>2</sub> and an oxygen evolution photocatalyst Bi<sub>20</sub>TiO<sub>32</sub> are prepared by ion-exchange reaction and a high-temperature quenching method, respectively.<sup>8-10</sup> Chemical precipitation method is another way of achieving metastable compounds. Preparation of hexagonal MoO<sub>3</sub> was realized by utilizing concentrated HCl solution as a precipitation agent.<sup>11</sup> Similarly, introducing ammonia solution into the metal precursor is the key step in the synthesis of tetragonal NiO-ZrO<sub>2</sub> solid solution.<sup>12</sup> In addition, mild reaction temperature (< 100 °C) as well as attainable scale-up are recognized as advantages of the precipitation route.<sup>13-15</sup>

Deep eutectic solvents (DESs) are emerging class of materials made by mixing hydrogen bond donor and acceptor. Eutectic composition of the constituents promotes significant melting point depression through hydrogen bonding.<sup>16-19</sup> Importantly, the resulting viscous liquid holds strong solvation capability of various metal precursors including binary oxides as well as metal salts, featuring DESs as suitable reaction mediums in preparation of functional metal oxides.<sup>20-25</sup> A combustion reaction involving thoroughly mixed metal precursors in DESs allows for control over a metal composition and particle size of the oxide compounds.<sup>20-25</sup> Furthermore, as a “designer solvent”, DESs provide synthetic tunability through a number of different combinations of hydrogen bond donor and acceptor, leading to variety of metal oxides accessible.<sup>20-27</sup> Versatility of DESs in oxide material syntheses have been further demonstrated by implementation of the solvent in the precipitation route. Without use of toxic reagents such as strong acid and base, size/morphology tunable binary metal oxides ZnO are achieved.<sup>28-31</sup> Considering simplicity of the experimental procedure and the great number of synthetic variables available to work with, the DES-involved precipitation route can potentially provide opportunities for new oxide material discovery.

With depletion of fossil fuels and their negative impact on our environments, development of new technology to reduce energy consumption/CO<sub>2</sub> emission and ultimately make use of sustainable fuel has become an urgent need. As a part of the eco-friendly movement, numerous efforts have been made to develop efficient semiconducting metal oxide materials for energy-related applications. For instance,

several vanadium oxides have been identified as a potential phosphor material in white light-emitting diodes (LEDs).<sup>32-36</sup> An intense broad band emission from 380 nm to ~800 nm with internal quantum efficiency of 79 % and 87 % was reported for RbVO<sub>3</sub> and CsVO<sub>3</sub>, respectively.<sup>32,33</sup> Zinc-rich compounds in the ZnO:V<sub>2</sub>O<sub>5</sub> system have shown to exhibit strong yellow (560 nm) luminescence.<sup>36</sup> In addition, some vanadium oxides have shown good light-harvesting properties, suitable for sustainable chemical fuel production via photoelectrochemical (PEC) water splitting.<sup>37-39</sup> Monoclinic BiVO<sub>4</sub> (band gap ~2.4 eV) exhibits quantum yield of 9 % with a photocatalytic oxygen evolution reaction (OER) rate of 421 μmol/h under visible light (> 420 nm) from a silver nitrate solution.<sup>37</sup> β-Mn<sub>2</sub>V<sub>2</sub>O<sub>7</sub> is another solar light absorber, possessing a band gap of 1.75 eV and suitable band alignment for both OER and the hydrogen evolution reaction (HER).<sup>38</sup> Here, we report an inimitable DES-involved precipitation synthesis route and properties of a metastable zinc-rich vanadate Zn<sub>4</sub>V<sub>2</sub>O<sub>9</sub>. We also discuss the reaction pathway and metastability of the zinc-rich compound. Finally, the electronic structure, optical absorption, vibrational properties, luminescence, surface photovoltage, and PEC characteristics of the compound are evaluated with various experimental and theoretical techniques.

## Experimental

**Material Synthesis.** ZnO (Alfa, 99.9%), V<sub>2</sub>O<sub>5</sub> (Alfa, 99.6% min), and urea (Alfa, 99%, crystalline) were used without purification. Choline chloride (Sigma-Aldrich, ≥98%) was dried under vacuum at 120 °C before the synthesis. A deep eutectic solvent (DES) was prepared by combining urea and choline chloride in a 2:1 molar ratio (54.322 g of urea and 63.750 g of choline chloride) in a Parafilm-covered glass beaker. The mixture was heated at 70 °C with stirring until a clear viscous liquid was obtained. The binary metal oxides (0.567 g ZnO and 0.633 g V<sub>2</sub>O<sub>5</sub> for Zn:V=1:1) were then dissolved in the solvent at 70 °C under vigorous stirring. For the various Zn:V ratio (2:1, 1.5:1, 1:1, 1:2), amount of the V<sub>2</sub>O<sub>5</sub> dissolved in the solvent was the same, but different amounts of ZnO were dissolved. 90 ml of deionized (DI) water (0 °C, 25 °C, 70 °C) was added to the 10 g of precursor-containing solution being kept at 70 °C with stirring. For a fast addition, the DI water was poured all at once with vigorous stirring. The DI water was added dropwise over a span of 3 hours using a burette without stirring for a slow addition. After the water was added, the reaction mixture was left without stirring at room temperature for 1 day. The resulting precipitates were decanted and washed with DI water three times followed by drying at 65 °C. For the synthesis of ZnO/Zn<sub>3</sub>V<sub>2</sub>O<sub>8</sub> and Zn<sub>4</sub>V<sub>2</sub>O<sub>9</sub>, the dried precipitate was heated at 400 °C for 6 hours and 837 °C for 30 seconds, respectively. About 43 mg of light-yellow powders (ZnO/Zn<sub>3</sub>V<sub>2</sub>O<sub>8</sub> and Zn<sub>4</sub>V<sub>2</sub>O<sub>9</sub> each) were obtained from the precursor solution with Zn:V ratio of 1:1 and used for all the characterizations unless otherwise noted. All heat treatments were performed with a heating rate of 10 °C/min in a fused quartz boat in air using a muffle furnace (box-type).

## **Characterization.**

### *Powder X-ray Diffraction.*

Synthesized samples were inspected by powder X-ray diffraction (PXRD) using a Rigaku Miniflex 600 diffractometer with Cu K $\alpha$  radiation ( $\lambda = 1.54051 \text{ \AA}$ ) and Ni K $\beta$  filter. Diffraction scans were collected on a zero-background plate at room temperature in air. PDXL software with the PDF-2 database was used for phase analysis.<sup>40</sup>

### *In Situ High Temperature Synchrotron Powder X-ray Diffraction.*

High-temperature synchrotron powder X-ray diffraction (HT-PXRD) scans were collected at the 17-BM beamline at the Advanced Photon Source (APS), Argonne National Laboratory (ANL), with an average wavelength  $\lambda = 0.24158 \text{ \AA}$  and  $0.24117 \text{ \AA}$  for the precipitate (from the precursor solution with Zn:V=1.5:1) and as-synthesized Zn<sub>4</sub>V<sub>2</sub>O<sub>9</sub>, respectively. The powder samples described in the Material Synthesis section were loaded into a silica capillary with 0.5 mm inner diameter and 0.7 mm outer diameter. Then, a secondary shield capillary (0.9 mm inner diameter and 1.1 mm outer diameter) in which the sample-filled capillary was placed was mounted in a flow furnace. A thermocouple was set as close as possible to the sealed end of the inner silica capillary, and the gas mixture (20% oxygen gas in helium gas) flowed into the open end of the inner capillary during the measurement. Details of the experimental setup can be found elsewhere.<sup>41</sup> The experiment was conducted in the temperature range from 23 °C to 900 °C. For the precipitate, heating rates of 50 °C/min and 10 °C/min up to 200 °C and 900 °C, respectively were employed with a cooling rate of 20 °C/min. For the as-synthesized Zn<sub>4</sub>V<sub>2</sub>O<sub>9</sub>, a heating/cooling rate of 10 °C/min was used. Rietveld refinement was performed using the GSAS software.<sup>42</sup>

### *Differential Scanning Calorimetry (DSC) and Thermogravimetric analysis (TGA).*

The DSC/TGA experiment was performed using a Netzsch STA449 F1 Jupiter coupled with a Netzsch quadrupole mass spectrometer 403 D Aeolos and a Bruker Tensor 37 FTIR spectrometer. A 5 mg of the precipitate powder (from the precursor solution with Zn:V=1:2) was loaded into a pan-type alumina (Al<sub>2</sub>O<sub>3</sub>) crucible with an alumina cover. The sample was heated from 40 to 850 °C and subsequently cooled to 282 °C with a rate of 10 °C/min under a constant flow of synthetic air (20% O<sub>2</sub> and 80% N<sub>2</sub>).

### *Scanning Electron Microscopy and Energy Dispersive Spectroscopy.*

Scanning electron microscopy (SEM) was carried out using a FEI Quanta 250 field emission SEM at 15 kV. Elemental composition analysis was performed with energy dispersive X-ray spectroscopy (EDS) by

means of an Oxford X-Max 80 detector. Powder samples were deposited on a carbon-taped SEM sample holder, followed by coating with 5 nm of iridium metal.

#### *X-ray Photoelectron Spectroscopy (XPS).*

A Kratos Amicus/ESCA 3400 instrument was used for XPS measurements. Samples were irradiated using Mg K $\alpha$  X-rays (240 W nonmonochromated) with the pass energy set at 150 eV. Photoelectrons emitted at 0° from the surface normal were energy analyzed with a DuPont type analyzer. CasaXPS was used for the processing of raw data files, and a Shirley baseline was applied to all spectra. The charge correction of XPS spectra were made by setting the adventitious C 1s peak to a binding energy of 284.8 eV. XPS data of V<sub>2</sub>O<sub>5</sub> (Alfa, 99.99%) was also collected as a reference.

#### *Raman spectroscopy.*

An XploRA confocal Raman microscope (HORIBA Scientific, Edison, NJ) was used with a 532nm laser operating at 1.3 mW. All samples were placed onto a coverslip directly and a 50 $\times$  objective (0.5 NA) was used. Three randomly selected locations were checked for each sample with a 30s acquisition and 3 accumulations. The spectra were averaged and plotted in Origin.

#### *Computational procedure.*

First principles calculations on Zn<sub>4</sub>V<sub>2</sub>O<sub>9</sub> were performed using *ab initio* density functional theory (DFT) as implemented in the Vienna *ab initio* Simulation Package (VASP).<sup>43</sup> All calculations employed a plane-wave basis set with projector-augmented wave (PAW) pseudopotentials.<sup>44</sup> The electronic structure of Zn<sub>4</sub>V<sub>2</sub>O<sub>9</sub> was calculated by using the Hyded-Scuseria-Ernzerhof screen hybrid exchange and correlation functional, HSE06, which implements a 75%:25% mixture of the Perdew-Burke-Ernzerhof (PBE):Hartree Fock functionals with a range separation of 0.2Å.<sup>45</sup> The electronic convergence criterion and ionic convergence criterion was set to 1 $\times$ 10<sup>-8</sup> eV and 1 $\times$ 10<sup>-6</sup> eV/Å, respectively. An energy cutoff of 500 eV was used and the first Brillouin zone was described by a Monkhorst-Pack *k*-point grid of 4 $\times$ 6 $\times$ 6, or  $\approx$ 1000 *k*-points/atom.<sup>46</sup> Phonon dispersion curves were calculated using the modified Parlinski-Li-Kawazoe *ab initio* force constant method as detailed in the PHONOPY package.<sup>47</sup> The phonons at the  $\Gamma$ -point and macroscopic dielectric tensor were necessary to calculate the Raman spectrum of Zn<sub>4</sub>V<sub>2</sub>O<sub>9</sub> according to the open source code vasp\_raman.py made available by Fonari and Stauffer.<sup>48</sup>

#### *Photoluminescence (PL) spectroscopy.*

#### *Diffuse reflectance UV-vis spectroscopy.*

Diffuse reflectance UV–vis absorption spectrum was collected using an SL1 tungsten halogen lamp (visIR), a SL3 deuterium lamp (UV), and a BLACK-Comet C-SR-100 spectrometer. A flattened and compressed powder samples were prepared on a glass slide for the measurement. A band gap value was estimated with a Tauc method by plotting  $(Abs \times hv)^{1/r}$  vs  $hv$ , where  $Abs$  is absorbance,  $hv$  is the excitation energy in eV, and  $r = 2$  for indirect allowed transitions.

#### *Surface Photovoltage Spectra (SPS).*

SPS data was measured using a circular (2.5 mm diameter), semitransparent vibrating gold mesh disk (*Kelvin Probe S, Besocke Delta Phi*) controlled by using a Kelvin Control 7 oscillator/amplifier (*Besocke Delta Phi*) and mounted inside of a home-built vacuum chamber evacuated to  $1.9 \times 10^{-4}$  mbar. Samples were prepared by dropcoating an aqueous suspension of the vanadate on fluorine-doped tin oxide (FTO) followed by [annealing at 500 °C in air for 2 h](#), and were placed 1.0 mm underneath the Kelvin probe and connected electrically to the ground, as reported previously.<sup>49</sup> Illumination in the 0.8 eV–4.13 eV regime was provided by light from a 150 W Xe lamp (Perkin Elmer) and filtered through an Oriel Cornerstone 130 monochromator. The light exiting the monochromator had a FWHM (full-width/half-maximum) of 8 nm–15 nm, depending on the wavelength, and the intensity at the sample was  $150 \mu\text{W}/\text{cm}^2$  on average. Spectra were acquired by stepping the photon energy by 0.0124 eV every 5 s and by measuring the contact potential difference (CPD) value at each step. CPD values are reported relative to the CPD value in the dark. Positive values correspond to electrons moving toward the Kelvin probe and negative values correspond to electrons moving away from the Kelvin probe. To correct for drift effects, a baseline was established by measuring CPD values in the dark for at least 15 min before each scan and by fitting the CPD values to a linear graph, which was then subtracted from the raw data.

#### *Photoelectrochemical (PEC) Measurements.*

A three-electrode setup was used in the PEC measurements. A Pt wire and Hg/Hg<sub>2</sub>Cl<sub>2</sub> in 1.0 M KCl were used as the counter and reference electrodes, respectively, and a 0.1 M Na<sub>2</sub>SO<sub>4</sub> aqueous solution with 20 % methanol (pH 7), or 0.1 M K<sub>2</sub>SO<sub>4</sub> (pH 7) served as the electrolyte. PEC measurements were performed after purging the electrolyte with N<sub>2</sub> for 10 minutes. Potentials were converted to normal hydrogen electrode (NHE) after cell calibration with a K<sub>3/4</sub>Fe(CN)<sub>6</sub> redox couple ( $E^0=0.358$  V). For water oxidation, potentials were further converted to reversible hydrogen electrode (RHE) according to the pH of electrolyte. A 300 W Xe lamp served as the visible light source. The light intensity at the electrode was  $100 \text{ mW}\cdot\text{cm}^{-2}$ , as measured with a GaAsP photodetector connected to a ILT 1400 light meter from International Light Technologies. Electrodes of Zn<sub>4</sub>V<sub>2</sub>O<sub>9</sub> were fabricated by drop-casting 0.6 mL aqueous suspension (ca. 3

mg/mL) onto fluorine-doped tin oxide (FTO) glasses ( $0.385 \text{ cm}^{-2}$ ), followed by drying in air, and annealing at  $500 \text{ }^\circ\text{C}$  in air for 2 h.

## Result and discussion

### *Crystal Structure*

$\text{Zn}_4\text{V}_2\text{O}_9$  is the most Zn-rich oxide in the ZnO- $\text{V}_2\text{O}_5$  pseudo binary system and has structural similarities to zinc hydroxy vanadate hydrate  $\text{Zn}_3(\text{OH})_2\text{V}_2\text{O}_7 \cdot 2\text{H}_2\text{O}$  and another zinc-rich vanadate  $\text{Zn}_3\text{V}_2\text{O}_8$ . The crystal structure of  $\text{Zn}_3(\text{OH})_2\text{V}_2\text{O}_7 \cdot 2\text{H}_2\text{O}$  has trigonal symmetry ( $P\bar{3}m1$ ) and is composed of edge-sharing zinc oxide/hydroxide octahedra,  $\text{ZnO}_4(\text{OH})_2$ , building a Brucite-type ( $\text{Mg}(\text{OH})_2$ ) layer stacked along the  $c$ -axis (Figure 1a).<sup>50-52</sup> The three of four octahedral sites in the close-packed layer of oxygen atoms are occupied by zinc atoms.<sup>50-52</sup> The remaining site is surrounded by vanadium tetrahedra, building a Kagome lattice with hexagonal void space.<sup>50-52</sup> V-O-V pillars within pyrovanadate ( $[\text{V}_2\text{O}_7]^{4-}$ ) group keep the layers apart, creating a porous framework with interlayer spacing of  $7.231 \text{ \AA}$ .<sup>43-45</sup> The large cavities are randomly filled by water molecules, which form hydrogen bonds with OH groups in the zinc oxide/hydroxide polyhedra.<sup>50-52</sup>  $\text{Zn}_3\text{V}_2\text{O}_8$  crystallizes in orthorhombic space group  $Cmca$ .<sup>53</sup> The edge-sharing  $[\text{ZnO}_6]$  octahedra forms Kagome layers, made of corner-sharing triangles and hexagonal voids, along the  $c$ -axis (Figure 1b).<sup>53</sup> Unlike the flat Kagome lattice seen in  $\text{Zn}_3(\text{OH})_2\text{V}_2\text{O}_7 \cdot 2\text{H}_2\text{O}$ , the layers in  $\text{Zn}_3\text{V}_2\text{O}_8$  are buckled and thus provide a staircase geometry.<sup>53</sup>  $\text{VO}_4$  tetrahedra allows the isolated layers to be stacked along the  $b$ -axis.<sup>53</sup> With the most zinc-rich composition,  $\text{Zn}_4\text{V}_2\text{O}_9$  crystallizes in monoclinic space group of  $P2_1$ .<sup>54</sup> Out of eight crystallographically independent zinc atoms, five of them are 5-coordinated and the rests (Zn(3), Zn(6), and Zn(8)) are 4-coordinated (Figure 1c-d).<sup>54</sup> On the other hand, all four unique vanadium atoms are tetrahedrally coordinated.<sup>54</sup> The  $[\text{ZnO}_5]^{8-}$  triangular bipyramids and  $[\text{Zn}(3)\text{O}_4]$  tetrahedra share edges and corners to construct layers along the  $c$ -axis (Figure 1d, left).<sup>54</sup> Similar to the buckled Kagome layers in  $\text{Zn}_3\text{V}_2\text{O}_8$ ,  $\text{Zn}_4\text{V}_2\text{O}_9$  holds void spaces within its layer but with more variety: rectangular, hexagonal, and octagonal nets (Figure 1c, right).<sup>54</sup> The space between the layers is occupied by  $[\text{Zn}(6)\text{O}_4]$  and  $[\text{Zn}(8)\text{O}_4]$  tetrahedra as well as  $[\text{VO}_4]$  tetrahedra (Figure 1d, right).<sup>54</sup>

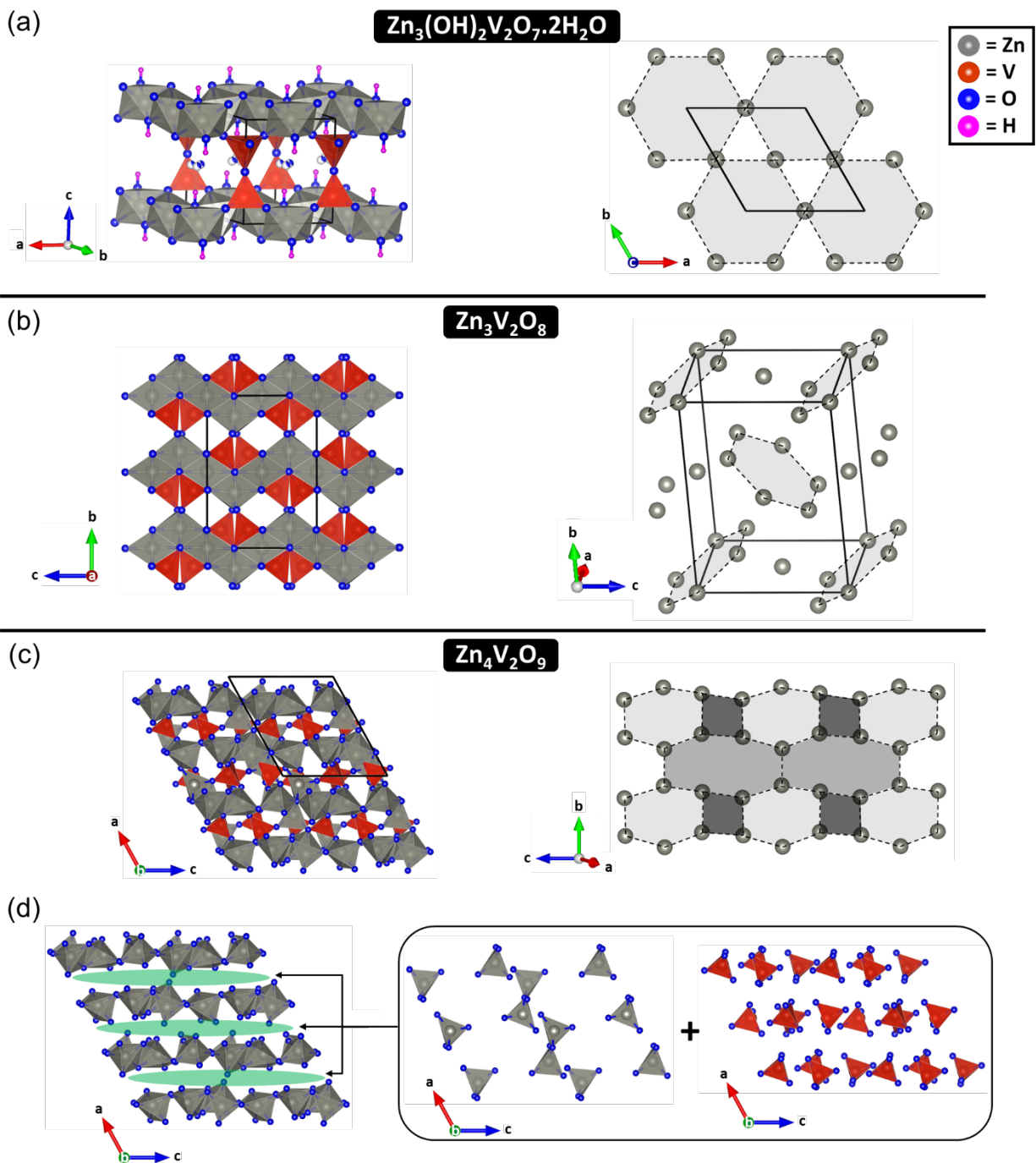


Figure 1. Crystal structure of  $\text{Zn}_3(\text{OH})_2\text{V}_2\text{O}_7 \cdot 2\text{H}_2\text{O}$  (a),  $\text{Zn}_3\text{V}_2\text{O}_8$  (b) and  $\text{Zn}_4\text{V}_2\text{O}_9$  (c). Gray spheres in the figures to the right indicate positions of Zn atoms.

### Synthesis.

A deep eutectic solvent (DES) comprised of urea (hydrogen bond donor, m.p.132-135 °C) and choline chloride (hydrogen bond acceptor, m.p. 302 °C) is employed for the synthesis of zinc-rich vanadates. With

the eutectic composition (urea : choline chloride = 2 : 1), the mixture exhibits a significantly low melting point ( $\sim 30$  °C) due to a strong hydrogen bonding interaction between the components.<sup>16-19</sup> Importantly, stable binary transition metal oxides, such as ZnO and V<sub>2</sub>O<sub>5</sub>, are utilized as metal precursors in this study because of appreciable solubility in the choline chloride-urea DES: 1.31 M for ZnO at 70 °C and 0.030 M for V<sub>2</sub>O<sub>5</sub> at 50 °C.<sup>55</sup> The preparation of precursor solution involves formation of metal-DES complexes — [ZnClO·urea]<sup>+</sup> and [VO<sub>2</sub>Cl<sub>2</sub>]<sup>-</sup> — upon dissolution,<sup>55</sup> providing a great atom economy in the metal oxide synthesis. When the binary metal precursors are fully dissolved in the eutectic mixture at 70 °C, a transparent solution is produced with color ranging from colorless to dark green depending on the amount of vanadium oxide dissolved. Deionized H<sub>2</sub>O, a precipitation agent (often called antisolvent), is then introduced to the precursor solution to obtain white precipitates. At the initial stage of antisolvent addition, the solution concentration gradually drops, and solutes eventually reach their solubility limit. With continuation of antisolvent addition, supersaturation is developed between the solubility curve and the metastable limit, at which nucleation proceeds spontaneously and rapidly.<sup>56-60</sup> Crystals then begin to grow if the supersaturation condition is maintained in the metastable zone with desired precipitation condition (e.g., low temperature).<sup>56-60</sup>

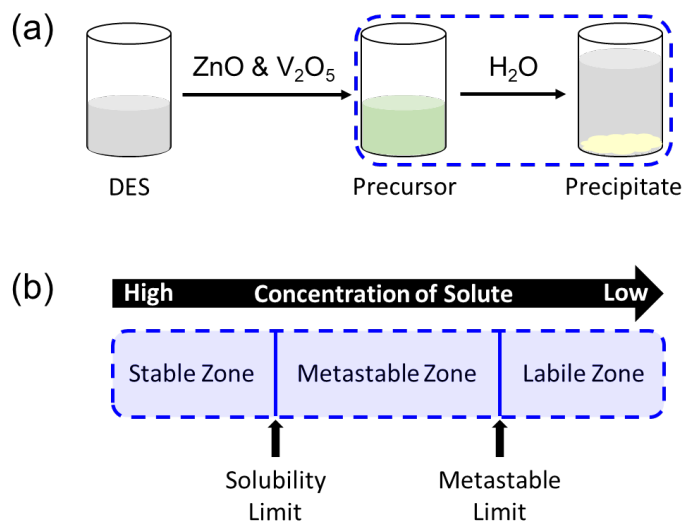


Figure 2. Visual description of the synthesis route used in this study (a) and a general precipitation process (b).

To understand the precipitation process, three different experimental parameters — initial metal-to-metal ratio in the solution, temperature of antisolvent, and antisolvent addition rate — were varied. Immediate addition of antisolvent is employed with temperature of precursor and antisolvent being kept at 70 °C and room temperature, respectively unless stated otherwise. Figure S1 shows powder X-ray diffraction patterns of precipitates obtained from the precursor solutions with various Zn/V ratios. All the powder samples

contain  $\text{Zn}_3(\text{OH})_2\text{V}_2\text{O}_7 \cdot 2\text{H}_2\text{O}$  (ICSD 59251) as a main phase with a small unknown impurity appearing at  $\sim 13$  degrees (marked with an asterisk). Phase identification based on such a weak and broad diffraction peak is limited. However, position of the unknown peak matches well with that of the most intense diffraction peak of zinc carbonate hydroxide,  $\text{Zn}_5(\text{OH})_6(\text{CO}_3)_2$  (ICSD 16583), which can be formed from the reaction between  $\text{Zn}^{2+}$  and urea.<sup>30</sup> The energy dispersive X-ray spectroscopy (EDS) mapping shows homogeneous distribution of Zn, V, and O throughout all the powder samples (Figure S2). In addition, the average molar ratio of Zn:V from all samples is determined to be  $\sim 2:1$  from the quantitative X-ray analysis of multiple spots within the precipitate powders. Thus, we conclude that the zinc dihydroxide divanadate dihydrate together with an additional zinc-containing source are precipitated independently of metal ratios in the precursor solution. Interestingly, we do not see any crystalline binary oxide phases such as ZnO,  $\text{VO}_2$ ,  $\text{V}_2\text{O}_3$ , and  $\text{V}_2\text{O}_5$  although the precipitation route using DES was reported to be a way to obtain binary metal oxides.<sup>28-31</sup> By adding water and/or ethanol antisolvent to the ZnO dissolved in the mixture of urea and choline chloride, Dong et al. prepared the zinc oxide nanoparticles with various morphology.<sup>28-30</sup> Similarly,  $\text{Cu}^{2+}$ -doped ZnO was obtained via the precipitation process by using copper nitrate as a dopant added in the antisolvent, consisting of a ethylene glycol and deionized water mixture.<sup>31</sup> We, for the first time, demonstrate that the ternary metal hydroxy oxide phase can be achieved by this route. It is noticeable that the synthesis of  $\text{Zn}_3(\text{OH})_2\text{V}_2\text{O}_7 \cdot 2\text{H}_2\text{O}$  usually requires a heat treatment under hydrothermal or microwave conditions.<sup>50-52, 61-65</sup> Accordingly, we believe that the precipitation process lowers the formation energy of the ternary zinc dihydroxide divanadate dihydrate phase.

Another parameter — temperature of antisolvent — is investigated for its impact on formation of the crystalline phase and size/morphology of particles precipitated. Precipitates obtained with antisolvent at different temperatures have almost identical powder X-ray diffraction patterns with the  $\text{Zn}_3(\text{OH})_2\text{V}_2\text{O}_7 \cdot 2\text{H}_2\text{O}$  as a main phase (Figure S3). Various sizes of agglomerates made of 2D irregular-shaped nanosheets are observed from the precipitates. Notably, antisolvent at low temperature yields bigger individual particles as compared to that obtained with the higher temperature of antisolvent (Figure S3). These finding shares similarity with a report about controlling size of Co nanoparticles based on the temperature of oleic acid in dichlorobenzene solution where  $\text{Co}_2(\text{CO})_8$  precursor was injected into.<sup>66</sup> When a lower temperature precursor solution was injected, larger cobalt particles with broad size distributions formed.<sup>66</sup> A quick addition method is also one of the crucial parameters in obtaining nano-sized particles. Therefore, fast injection method with varying temperature of antisolvent controls particles size within the nano regime.

We investigated an addition rate of antisolvent as the third parameter for the precipitation process. The main diffraction peaks of precipitates obtained from both slow and fast addition methods are indexed to the  $\text{Zn}_3(\text{OH})_2\text{V}_2\text{O}_7 \cdot 2\text{H}_2\text{O}$  (Figure 3). The SEM image of fast addition method shows the irregular shaped

aggregates made of nanosheets with thickness of a few nanometer. In contrast, the slow addition method produces a bouquet-shaped agglomerates. The sheet-like individual particles have a similar thickness as those from the fast addition method. However, the exfoliated individual particles form micron-sized three-dimensional flower-like morphology. When the room temperature solvent is added fast to the precursor solution, the reaction mixture rapidly reaches the labile zone beyond the metastable limit. Thus, the immediate precipitation occurs with a fast nucleation rate, which is responsible for the resulting small particles. On the other hand, the slow addition method allows the supersaturation (from low to high concentration level) to be maintained in the metastable zone for extended hours. The dropwise addition helps keeping the reaction mixture to remain at the warm temperature (70 °C). As a result, significantly slower nucleation rate is achieved followed by particles' growth with time. The different morphology/size of particles observed by SEM is validated by the PXRD results (Figure 3a). First, the shift of the most intense diffraction peak to the lower diffraction angles is observed from the fast addition method. Considering water molecule is randomly occupied within the channel,<sup>50-52</sup> the difference in the diffraction peak position could indicate that the amount of adsorbed H<sub>2</sub>O molecule can vary depending on the antisolvent addition rate — the fast addition rate results in expanding the interlayer spacing by ~ 4.1 % as compared to the slow addition method (inset to Figure 3a). Thus, the chemical formula of the zinc hydroxy vanadate hydrate should be modified to Zn<sub>3</sub>(OH)<sub>2</sub>V<sub>2</sub>O<sub>7</sub>·nH<sub>2</sub>O (n ≥ 0). We can understand the variation in interlayer distance based on the structural similarity between β-alumina and the Zn<sub>3</sub>(OH)<sub>2</sub>V<sub>2</sub>O<sub>7</sub>·nH<sub>2</sub>O. The β-alumina, (M<sub>2</sub>O)<sub>x</sub>·11Al<sub>2</sub>O<sub>3</sub> (M = monovalent cation, 1.2 < x < 1.3) has a layered structure with spinel blocks made of [AlO<sub>4</sub>] tetrahedra and [AlO<sub>6</sub>] octahedra.<sup>67-69</sup> Reminiscent of the V-O-V pillar in the Zn<sub>3</sub>(OH)<sub>2</sub>V<sub>2</sub>O<sub>7</sub>·nH<sub>2</sub>O, Al-O-Al bonds separate the spinel blocks of the β-alumina creating a rigid framework.<sup>67-69</sup> Various monovalent cations can occupy the interlayer spacing within the channel.<sup>67-69</sup> Likewise, the open framework within zinc dihydroxide divanadate can host different molecular species other than water molecules. The observed expansion of interlayer distance, thus, could be due to presence of additional molecular species from the choline chloride-urea mixture trapped in the channel. We also noticed that the relative intensity of diffraction peaks varies depending on the antisolvent addition rate. Unlike the slow addition method, the PXRD pattern of fast addition method shows significantly enhanced peak intensities for (100), (200), and (110) planes. We can deduce that the nanosheets are oriented along the [100] and [110] directions corresponding to the extended layers of zinc oxide/hydroxide octahedra and the face diagonal of the trigonal unit cell, respectively. Therefore, we conclude that the nanosheets are grown anisotropically, resulting in the significant preferred orientation. In addition, we noticed that {h00} diffraction peaks of the two PXRD patterns have a similar full width at half maximum (FWHM), indicating thickness of individual sheets are alike: ~ 29.8 nm calculated by Scherrer equation. However, other peaks corresponding to (101), (111), and (201) planes have noticeably broadened peak widths for the fast addition

method as compared to that of slow addition method. Based on the anisotropic crystal growth along the [100] together with a diffraction peak broadening stemming from a decrease in crystalline domain size, our finding suggests that the two-dimensional nanosheets of smaller size are produced by the fast addition method.

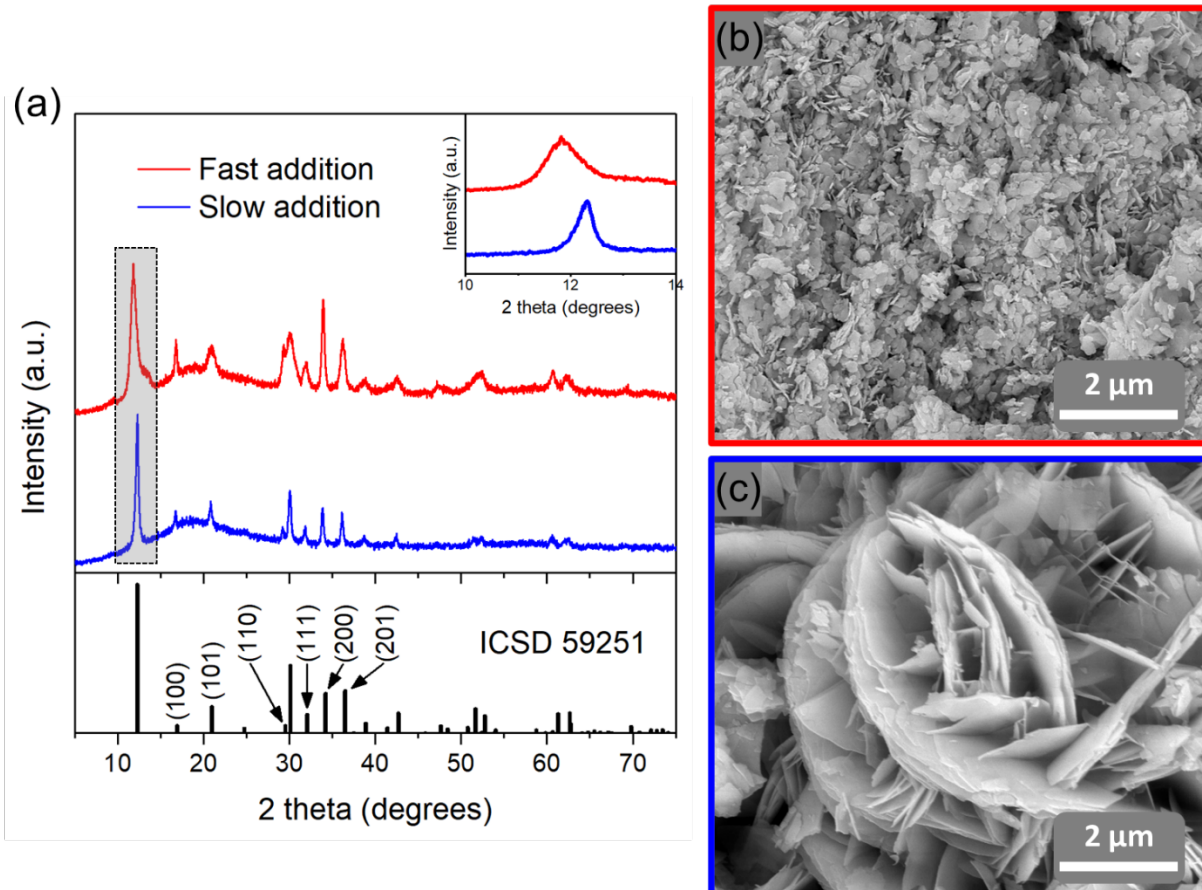


Figure 3. PXRD patterns (a) and SEM images (b) of the  $\text{Zn}_3(\text{OH})_2\text{V}_2\text{O}_7 \cdot 2\text{H}_2\text{O}$  precipitates from two different antisolvent addition rates. ICSD 59251 indicating the  $\text{Zn}_3(\text{OH})_2\text{V}_2\text{O}_7 \cdot 2\text{H}_2\text{O}$  phase.

According to the previous reports, preparation of  $\text{Zn}_3\text{V}_2\text{O}_8$  is readily available by heat treatment of  $\text{Zn}_3(\text{OH})_2\text{V}_2\text{O}_7 \cdot 2\text{H}_2\text{O}$  between 200 °C and 500 °C where dehydration occurs.<sup>62-63</sup> The PXRD data of sample after annealing of the precipitate at 400°C in air (Figure 4a) agrees with the literature data as the diffraction peaks correspond to  $\text{Zn}_3\text{V}_2\text{O}_8$  (ICSD 23776), albeit the phase has low crystallinity. Change in dwelling time does not have impact on the crystalline phase observed. However, the pronounced shift of peaks at ~43 and 62° 2θ to lower diffraction angle is observed, likely due to an expanded unit cell. Interestingly, the SEM image of  $\text{Zn}_3\text{V}_2\text{O}_8$  show that size and morphology of the nanosheets remain unaltered before and after the heat treatment. Based on the homogeneous distribution of Zn and V from the elemental EDS maps (Figure

S4) together with absence of crystalline diffraction peak of secondary phases, we hypothesize that amorphous ZnO is deposited on the host material  $\text{Zn}_3\text{V}_2\text{O}_8$  from the heating of precipitate.

With further heating of the precipitate, we obtained another zinc-rich vanadate. The powder X-ray diffraction peaks of sample after annealing of the precipitate at  $837^\circ\text{C}$  are indexed to  $\text{Zn}_4\text{V}_2\text{O}_9$  (ICSD 59109) as shown in Figure 4b. It should be noted that the purity of the powder sample varies depending on the Zn/V ratio in the precursor solution (Figure S5). The synthetic condition with the 1:1 ratio of Zn/V yields phase-pure sample whereas contamination with ZnO is observed when the zinc-rich or vanadium-rich compositions are loaded as the precursor. Taking into account the fact that target compound  $\text{Zn}_4\text{V}_2\text{O}_9$  does not decompose at temperature below  $837^\circ\text{C}$ , as discussed further, we believe that presence of ZnO impurity is due to the excess zinc source  $\text{Zn}_5(\text{OH})_6(\text{CO}_3)_2$  precipitated upon the antisolvent addition. SEM image of  $\text{Zn}_4\text{V}_2\text{O}_9$  shows agglomerates sized up to  $\sim 27\ \mu\text{m}$  with the porous morphology. Densification and sintering are the most common phenomena of solid-state materials resulting from heat treatments. However, it has been reported that thermal decomposition of metal hydroxide such as  $\text{Ni}(\text{OH})_2$  and  $\text{Mg}(\text{OH})_2$  can lead to the formation of porous metal oxides NiO and MgO.<sup>70-72</sup> Therefore, the thermal dehydration of  $\text{Zn}_3(\text{OH})_2\text{V}_2\text{O}_7 \cdot 2\text{H}_2\text{O}$  is responsible for the porosity formation as shown in the Figure 4b.

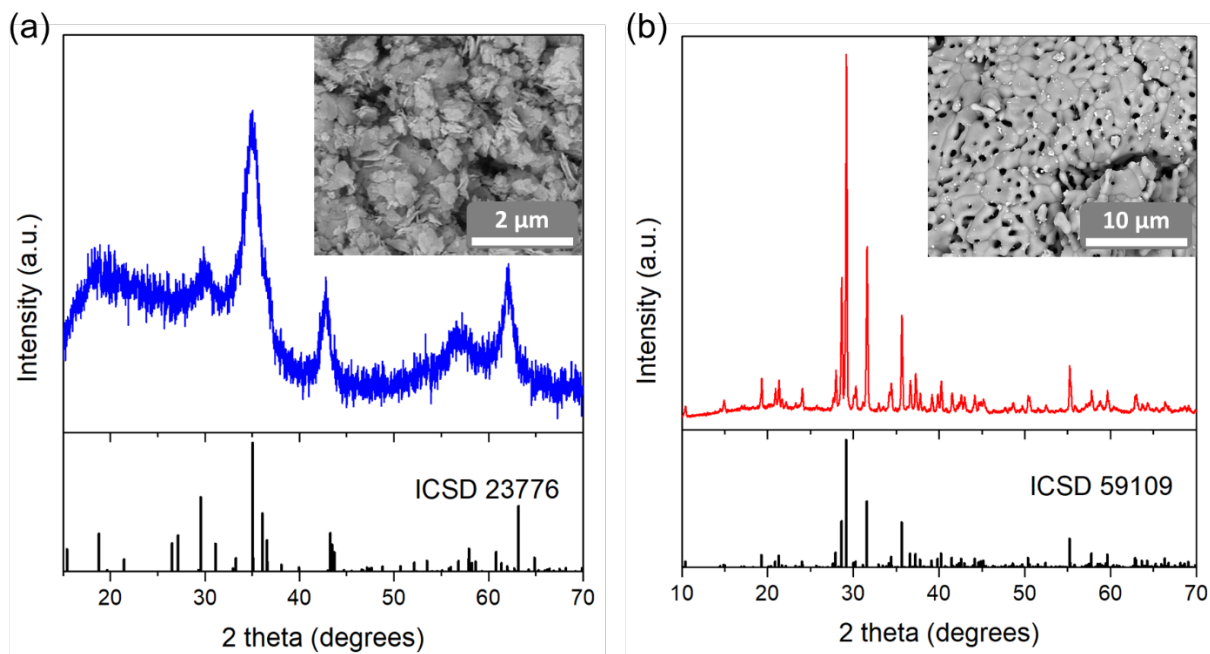


Figure 4. PXRD patterns and SEM images of ZnO/ $\text{Zn}_3\text{V}_2\text{O}_8$  (a) and  $\text{Zn}_4\text{V}_2\text{O}_9$  (b) obtained by heating the precipitate at  $400^\circ\text{C}$  and  $837^\circ\text{C}$ , respectively. ICSD 23776 and 59109 indicating the  $\text{Zn}_3\text{V}_2\text{O}_8$  and  $\text{Zn}_4\text{V}_2\text{O}_9$  phase, respectively.

We further investigated the reaction pathway towards zinc-rich vanadates using *in situ* high-temperature powder X-ray diffraction (HT-PXRD). Figure 5 shows phase evolution PXRD patterns upon heating of precipitate from room temperature to 473 °C. The starting material is composed of  $\text{Zn}_3(\text{OH})_2\text{V}_2\text{O}_7 \cdot 2\text{H}_2\text{O}$  as a major phase and tentatively  $\text{Zn}_5(\text{OH})_6(\text{CO}_3)_2$  (marked with an asterisk) as a minor phase. Notably, two overlapping peaks are observed at  $\sim 0.7 \text{ \AA}^{-1}$ , indicating the two different interlayer distances within the  $\text{Zn}_3(\text{OH})_2\text{V}_2\text{O}_7 \cdot 2\text{H}_2\text{O}$  (7.231 Å and 7.387 Å). Upon heating up to 185 °C, the diffraction peak at the lower Q value is gradually disappearing. According to the previous reports,<sup>51,52</sup> the adsorbed water can be thermally removed at 200 °C, so more than 50% of the volume between the layer is being unoccupied. The dehydrated product still preserves the layered structure with a contraction in the interlayer distance by less than 0.1 Å, indicating that the water is not critical to the structure.<sup>52</sup> Therefore, our experimental results suggest that deintercalation of water and an additional molecular species from the channel occurs at different rates upon heating while the layered structure is preserved. In turn, the intensity of the diffraction peak at the higher Q value corresponding to the interlayer distance of 7.231 Å begins to decrease above 200 °C when the layered structure supported by V-O-V pillars collapses.  $\text{Zn}_3(\text{OH})_2\text{V}_2\text{O}_7 \cdot 2\text{H}_2\text{O}$  phase finally disappears and broad diffraction peaks of  $\text{Zn}_3\text{V}_2\text{O}_8$  become dominant above 230 °C, validating formation of the oxide nanoparticles as evidenced from the *ex situ* experimental data (Figure 4a).

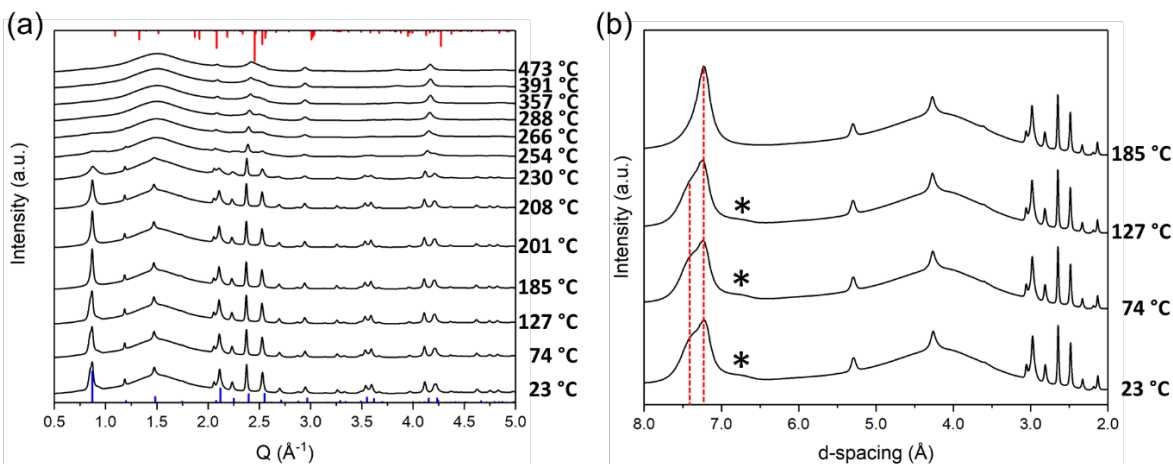


Figure 5. Selected high temperature powder diffraction patterns upon heating up to 473 °C with blue and red bars indicating calculated patterns of  $\text{Zn}_3(\text{OH})_2\text{V}_2\text{O}_7 \cdot 2\text{H}_2\text{O}$  (bottom) and  $\text{Zn}_3\text{V}_2\text{O}_8$  (top), respectively (a). Two overlapping diffraction peaks highlighted by red dotted lines (b).

The narrowing of diffraction peaks for  $\text{Zn}_3\text{V}_2\text{O}_8$  and ZnO are observed starting from 482 °C and 563 °C, respectively, suggesting the growth of crystals from nano to micron scale. Upon further heating up to 747 °C, there is no change in the observed diffraction patterns except for diffraction peaks shift stemming from thermal expansion. It should be noted that  $\text{Zn}_4\text{V}_2\text{O}_9$  starts to appear above 759 °C, and a significant increase

in its phase fraction is observed until 804 °C (Figure 6). On the other hand, fractions of  $\text{Zn}_3\text{V}_2\text{O}_8$  and  $\text{ZnO}$  gradually decrease within this temperature range, revealing that  $\text{Zn}_4\text{V}_2\text{O}_9$  is a product of the reaction between  $\text{Zn}_3\text{V}_2\text{O}_8$  and  $\text{ZnO}$  intermediates.  $\text{Zn}_4\text{V}_2\text{O}_9$  is thermally stable until 861 °C, above which  $\text{ZnO}$  phase fraction starts to increase due to decomposition of  $\text{Zn}_4\text{V}_2\text{O}_9$ . Another decomposition product,  $\text{Zn}_3\text{V}_2\text{O}_8$ , is not seen in the diffraction pattern because it is unstable above 800 °C.<sup>73</sup> We also noticed that a side product  $\text{Zn}_2\text{SiO}_4$  appears from 884 °C and stays until the end of the experiment due to the side reaction with the silica capillary material. Upon cooling from 900 °C, none of ternary zinc vanadate phases are observed until 840 °C, below which  $\text{Zn}_3\text{V}_2\text{O}_8$  starts to appear. However, the  $\text{Zn}_3\text{V}_2\text{O}_8$  is only stable until 548 °C, which could be due to the fast cooling rate (20 °C/min) employed. Diffraction peaks of another ternary zinc vanadate  $\beta\text{-Zn}_2\text{V}_2\text{O}_7$  show up below 823 °C and stay until the end of cooling. Importantly, the most zinc-rich phase  $\text{Zn}_4\text{V}_2\text{O}_9$  is not recovered after its complete decomposition although  $\text{Zn}_3\text{V}_2\text{O}_8$  and  $\text{ZnO}$  coexist in the powder sample upon cooling from 823 °C to 548 °C.

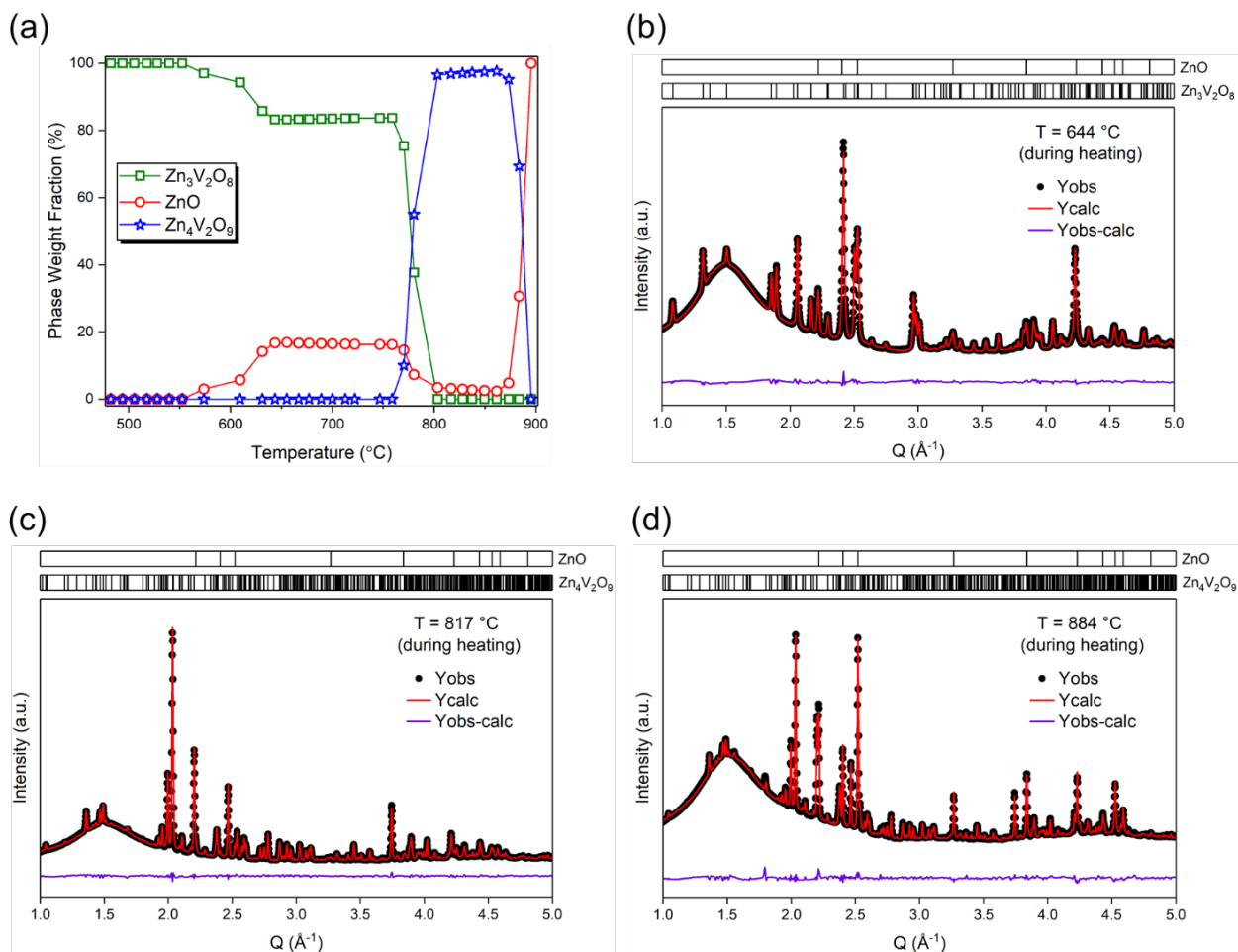
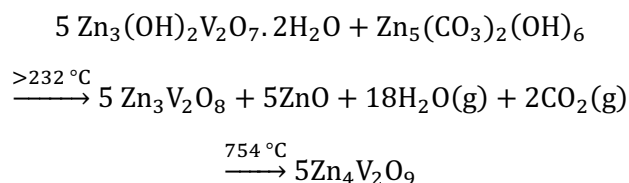


Figure 6. Summary of HT-PXRD data from sequential Rietveld refinements for the precipitate (a). The refinement results of selected diffraction patterns collected at different temperatures during heating (b-d). The side product  $\text{Zn}_2\text{SiO}_4$  is omitted for clarity.

Differential scanning calorimetry (DSC) and thermogravimetric analysis (TGA) of the precipitate support findings from HT-PXRD and provide more accurate determination for phase transformation temperatures (Figure 7). The first broad endothermic peak centered at 171 °C is observed along with the sample mass loss of ~ 9 %. The signals of m/z 17 and 18 from the mass spectrometer show the highest ion current at 184 °C and 169 °C, respectively, suggesting that the dehydration process from  $\text{Zn}_3(\text{OH})_2\text{V}_2\text{O}_7 \cdot 2\text{H}_2\text{O}$  contributes to the first thermal event. According to Shi et al., the water removal can occur from the temperature as low as 40 °C.<sup>62</sup> Therefore, our hypothesis is further supported by the gradual decrease in sample mass from 76 °C, which coincides with the gradual increase in m/z 17 and 18 intensity. Interestingly, another gas signal of m/z 44 begins to increase drastically from 153 °C and reaches its highest value at 174 °C. Since  $\text{Zn}_3(\text{OH})_2\text{V}_2\text{O}_7 \cdot 2\text{H}_2\text{O}$  holds a porous framework, the gas signal is likely from a fragment ion such as  $\text{CH}_3\text{CHNH}_2$  of additional molecular species trapped in the channel. Similarly, the signal m/z 30 can be understood by another fragmentation such as  $\text{CH}_2\text{NH}_2$ . The first broad exothermic peak at 232 °C is then attributed to the formation of  $\text{Zn}_3\text{V}_2\text{O}_8$  as seen in the previous report.<sup>62</sup> It should be noted that the ion currents of m/z 17 and 18 increase again from 221 °C and reach the local maximum at 237 °C. Sinhamahapatra et al. showed that  $\text{Zn}_5(\text{CO}_3)_2(\text{OH})_6$  undergoes thermal decomposition process in two steps: dehydration at 250 – 325 °C to yield  $\text{Zn}_5(\text{CO}_3)_2\text{O}_3$  followed by carbonate removal at 325 – 440 °C, leaving ZnO as a final product.<sup>74</sup> We, thus, hypothesized that the second increase in intensities of signal m/z 17 and 18 is due to the water removal from  $\text{Zn}_5(\text{CO}_3)_2(\text{OH})_6$ . The m/z 44 signal from 288 – 524 °C, which can be assigned to removing carbonate from  $\text{Zn}_5(\text{CO}_3)_2(\text{OH})_6$ , further supports our hypothesis. In turn, a group of exothermic peaks appear between 417–527 °C. Although individual assignments of them are limited due to the peak overlap, we can deduce from HT-PXRD data that the growth of  $\text{Zn}_3\text{V}_2\text{O}_8$  as well as ZnO crystallization contribute to the exothermic thermal events. Finally, the endothermic peak with the onset temperature of 754 °C is assigned to the formation of  $\text{Zn}_4\text{V}_2\text{O}_9$  from the reaction between  $\text{Zn}_3\text{V}_2\text{O}_8$  and ZnO. There is no measurable DSC signal or sample mass loss observed afterwards. Based on the HT-PXRD and DSC/TGA data, the suggested reaction pathway towards  $\text{Zn}_4\text{V}_2\text{O}_9$  formation is as follows:



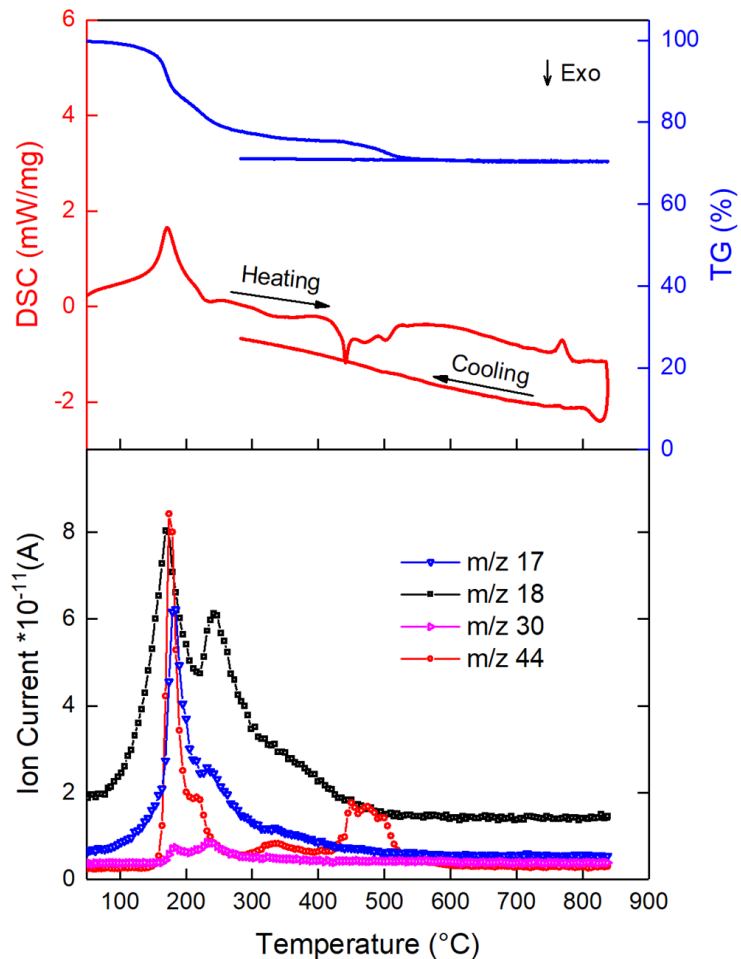


Figure 7. DSC/TGA upon heating and cooling of the precipitate (top). Released gas data collected using the mass spectrometer upon heating (bottom).

Obtaining the zinc-rich vanadate  $Zn_4V_2O_9$  has been a great challenge and required a tedious reaction procedure. Waburg et al. used a  $CO_2$ -laser generated flux and  $ZnO/V_2O_5$  mixture for the synthesis.<sup>54</sup> Even with a pelletized mixture of  $ZnO$  and  $V_2O_5$ , an extended period (60 – 72 hours) of sintering at 800 – 850 °C in air was required.<sup>75</sup> In addition, the reaction product had to be quenched in liquid nitrogen due to the metastable characteristic of  $Zn_4V_2O_9$ .<sup>75</sup> According to another report, heating the pre-made ternary oxide,  $Zn_3V_2O_8$ , mixed with  $ZnO$  at 835 °C followed by rapid quenching resulted in the formation of target compound.<sup>76</sup> However, a long reaction time (20 hours) at the elevated temperature was still a crucial step during the heat treatment.<sup>76</sup> In contrast, our synthetic method provides a complete reaction within 30 seconds of annealing of the precipitate at 837 °C and yields phase pure  $Zn_4V_2O_9$ . Such a fast reaction could stem from the labile precursor nanoparticles  $Zn_3(OH)_2V_2O_7 \cdot 2H_2O$  and  $Zn_5(CO_3)_2(OH)_6$  being well-mixed as supported by the elemental mapping. More specifically, the intermediate oxides  $Zn_3V_2O_8$  and  $ZnO$

derived from the precursors still maintain the intimate mixing, resulting in lowering of a diffusion barrier between the solids. It could also be possible that the intermediate oxides  $\text{Zn}_3\text{V}_2\text{O}_8$  and  $\text{ZnO}$  formed during the ramping stage of heating could have enhanced reactivity as compared to the pre-made counterparts. Therefore, we believe that suitable choice of precursors can potentially open a venue towards preparation of metastable materials. When it comes to cooling, we confirm that quenching of the reaction mixture is not necessary as there is no difference in the PXRD patterns obtained from quenching and slow natural-cooling methods (Figure S6). We further investigated the metastability of  $\text{Zn}_4\text{V}_2\text{O}_9$  using the *in situ* experiment. Figure S7 shows selected powder diffraction patterns of synthesized  $\text{Zn}_4\text{V}_2\text{O}_9$  upon heating followed by cooling. Thermal decomposition of the zinc-rich oxide phase is observed above  $880\text{ }^\circ\text{C}$  as expected from the HT PXRD data of the precipitate. It should be noted that cooling of the reaction mixture prior to complete decomposition of  $\text{Zn}_4\text{V}_2\text{O}_9$  leads to its phase recovery unlike the *in situ* experimental result of precipitate discussed earlier. Moreover, unknown diffraction peaks (marked with a transparent green box) appear at  $520\text{ }^\circ\text{C}$  and further grow until  $400\text{ }^\circ\text{C}$ . We conclude that the decomposition of  $\text{Zn}_4\text{V}_2\text{O}_9$  occurs at the specific temperature range ( $400 - 520\text{ }^\circ\text{C}$ ) upon cooling with a moderate rate ( $10\text{ }^\circ\text{C}/\text{min}$ ). *Ex situ* experimental data shown in Figure S8 additionally demonstrates metastable character of  $\text{Zn}_4\text{V}_2\text{O}_9$  — its thermal decomposition as a result of reheating at a particular temperature ( $650\text{ }^\circ\text{C}$ ) for 6 hours.

Raman spectroscopy is utilized to investigate vibrational properties of solid products. Figure 8 shows that the Raman spectrum of the precipitate agrees well with that of  $\text{Zn}_3(\text{OH})_2\text{V}_2\text{O}_7 \cdot 2\text{H}_2\text{O}$  reported in the literature<sup>77</sup> without any detectable peaks from binary metal oxides ( $\text{ZnO}$  and  $\text{V}_2\text{O}_5$ , see Figure S9). All the peaks can be understood by vibrations of  $[\text{V}_2\text{O}_7]^{4-}$  units.<sup>78</sup> The highest intensity from the band at  $863\text{ cm}^{-1}$  is assigned to the symmetric stretching mode of  $[\text{VO}_3]$ .<sup>78</sup> Combination of asymmetric stretching mode from  $[\text{VO}_3]$  and  $[\text{V-O-V}]$  is confirmed by the peak at  $795\text{ cm}^{-1}$ .<sup>78</sup> The Raman bands at  $475\text{ cm}^{-1}$  and  $427\text{ cm}^{-1}$  are attributed to asymmetric  $[\text{VO}_3]$  bending modes while a symmetric bending mode of  $[\text{VO}_3]$  is ascribed to the peak at  $325\text{ cm}^{-1}$ .<sup>78</sup> Furthermore, the  $[\text{V-O-V}]$  bending mode contributes to the Raman peak at  $249\text{ cm}^{-1}$ .<sup>78</sup> A weak broad band observed at  $\sim 927\text{ cm}^{-1}$  could arise from the strongest Raman peak of  $\text{Zn}_5(\text{CO}_3)_2(\text{OH})_6$  being shifted from  $1062\text{ cm}^{-1}$  due to its semicrystalline nature.<sup>79-81</sup> The Raman spectrum of the intermediate phase  $\text{ZnO}/\text{Zn}_3\text{V}_2\text{O}_8$  only shows a broad peak at  $786 - 873\text{ cm}^{-1}$  (Figure S9), which might be from the semicrystalline form of  $\text{Zn}_3\text{V}_2\text{O}_8$ .<sup>80-82</sup> The loss of long-range translational symmetry causes all phonons in the Brillouin zone to become Raman active, resulting in band broadening.<sup>80,81</sup>

The Raman spectrum of the synthesized  $\text{Zn}_4\text{V}_2\text{O}_9$  is shown in the Figure 8. With vanadium metal being exclusively in tetrahedral geometry, the observed Raman bands are assigned to vibration modes based on the free vanadate unit  $[\text{VO}_4]^{3-}$ .<sup>83</sup> Although the reduced symmetry of the vanadate tetrahedra in  $\text{Zn}_4\text{V}_2\text{O}_9$  removes degenerate vibration modes, all other modes are still Raman active.<sup>78</sup> The origin of peaks in the high wavenumber region ( $800 - 1000\text{ cm}^{-1}$ ) was reported to be the symmetric stretching mode of  $[\text{VO}_4]^{3-}$ .<sup>83</sup>

However, individual peak assignments was not available until now. With DFT calculated Raman active vibrational modes, we found out that each Raman peaks is mainly contributed by a stretching mode of a discrete V-O bond stemming from a particular vanadium coordination polyhedra (exception: 874, 792, and 766 $\text{cm}^{-1}$  as shown in Table 1). We, thus, conclude that the presence of four nonequivalent vanadium sites within the unit cell is responsible for the internal  $[\text{VO}_4]^{3-}$  modes splitting. The Raman peaks at 462  $\text{cm}^{-1}$  and 370  $\text{cm}^{-1}$  are assigned to asymmetric bending modes whereas the band at 285  $\text{cm}^{-1}$  is contributed by the symmetric bending mode.<sup>83</sup> Moreover, peaks corresponding to the lattice vibration modes appear at the low wavenumber region (80 – 250  $\text{cm}^{-1}$ ).<sup>83</sup>

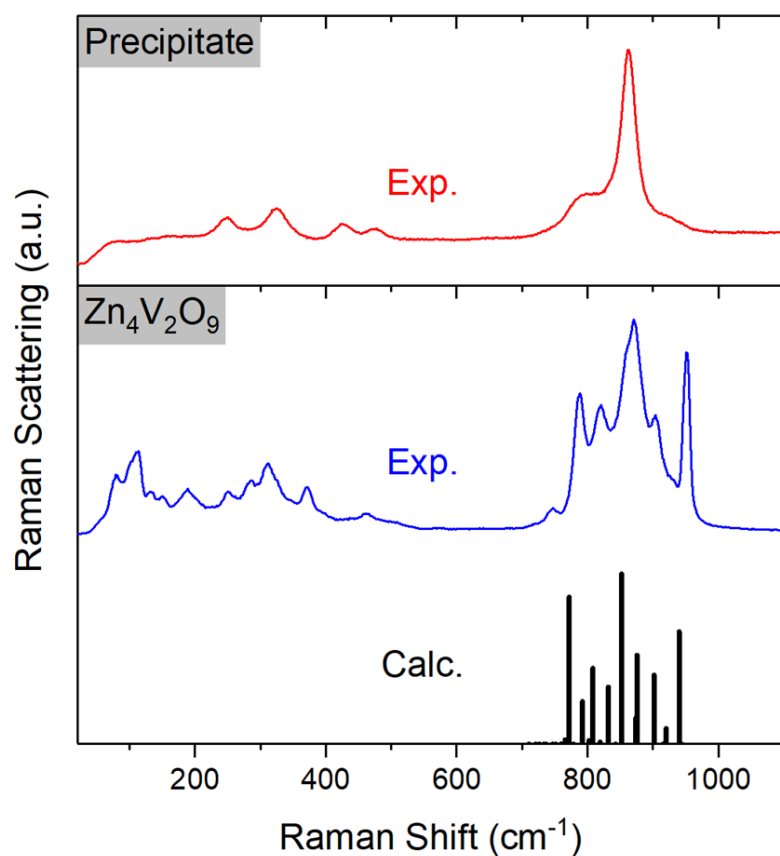


Figure 8. Experimental Raman spectra of the precipitate (top) and  $\text{Zn}_4\text{V}_2\text{O}_9$  (bottom). The calculated Raman active modes are shown in black bars.

Table 1. Experimental and Calculated Raman Data of Zn<sub>4</sub>V<sub>2</sub>O<sub>9</sub>.

Peak	Raman Shift (cm <sup>-1</sup> )		Calculated Raman Activity (arb. units)	Assignment
	Experiment	Calculation		
1	952	940 921	1991 335	$\nu(\text{V}_3\text{-O}_{11})$ $\nu(\text{V}_2\text{-O}_{17})$
2	903	902	1248	$\nu(\text{V}_4\text{-O}_{16})$
3	870	876 874 852	1590 523 2981	$\nu(\text{V}_2\text{-O}_{17})$ $\nu(\text{V}_1\text{-O}_{13}) + \nu(\text{V}_2\text{-O}_2)$ $\nu(\text{V}_1\text{-O}_{13})$
4	819	832 819 808	1045 103 1366	$\nu(\text{V}_1\text{-O}_1)$ $\nu(\text{V}_4\text{-O}_{14})$ $\nu^s(\text{O}_4\text{-V}_3\text{-O}_8)$
5	788	792 772	797 2583	$\nu^s(\text{O}_4\text{-V}_3\text{-O}_8) + \nu(\text{V}_2\text{-O}_{15})$ $\nu(\text{V}_4\text{-O}_{12})$
6	748	766	144	$\nu(\text{V}_2\text{-O}_2) + \nu(\text{V}_1\text{-O}_{14})$
7-8	462, 370	-	-	$\delta^{\text{as}}(\text{VO}_4)^{3-}$
9	285	-	-	$\delta^s(\text{VO}_4)^{3-}$
10-15	250, 188, 151, 132, 112, 80	-	-	Lattice vibrations

$\nu$ : bond-stretching vibration,  $\delta$ : angle-bending vibration s: symmetric, as: asymmetric. The assignments for peaks 7-15 are based on the previous report<sup>83</sup>.

To investigate the elemental composition and chemical state of metals and oxygen on the surface of Zn<sub>4</sub>V<sub>2</sub>O<sub>9</sub> and V<sub>2</sub>O<sub>5</sub> (reference sample), X-ray photoelectron spectroscopy (XPS) is carried out. The Zn 2p peaks together with Zn modified Auger parameter (2010.73 eV) from Zn<sub>4</sub>V<sub>2</sub>O<sub>9</sub> agree well with those of ZnO,<sup>84</sup> confirming that a divalent zinc cation is bonded to oxide anions (Figure S10). Figure 9 shows the O 1s and V 2p core level spectra in the binding energy range from 513 to 537 eV. The O1s peak is recognized as combination of two different species appearing at ~530.17 eV and ~531.87eV. The narrow peak at the low binding energy is ascribed to the lattice oxygen whereas the broad one at the high binding energy is due to presence of oxygen defects/surface adsorbed oxygen.<sup>85</sup> The spin-orbit splitting of V 2p<sub>3/2</sub> and V 2p<sub>1/2</sub> is observed in both samples. Considering peak positions and Coster-Kronig effect,<sup>84,86</sup> the symmetric peaks at ~517.37 eV with FWHM (full width at half maximum) of 1.38 eV (V 2p<sub>3/2</sub>) and at ~524.74 eV (FWHM=2.50 eV, V 2p<sub>1/2</sub>) from the reference V<sub>2</sub>O<sub>5</sub> indicate that vanadium is in the pentavalent state. On the other hand, Zn<sub>4</sub>V<sub>2</sub>O<sub>9</sub> shows a significant peak broadening: FWHMs of 2.66 eV and 5.82 eV for V 2p<sub>3/2</sub> and V 2p<sub>1/2</sub>, respectively. Such a wide peak suggests that a multiplet structure of vanadium cation is available due to unpaired electrons.<sup>84</sup> Based on the peak position (517.26 eV for V 2p<sub>3/2</sub>), however, we can

deduce that  $V^{5+}$  also exists. A reasonable deconvolution of the V 2p peaks is achieved with two pairs of spin-orbit doublets: peaks at 517.8 eV (FWHM = 1.78 eV) and 525.2 eV (FWHM = 2.70 eV) corresponding to V 2p<sub>3/2</sub> and V 2p<sub>1/2</sub> of  $V^{5+}$ , while the other two peaks at 516.6 eV (FWHM = 2.59 eV) and 524.2 eV (FWHM = 3.25 eV) indicating the reduced oxidation state of vanadium,  $V^{4+}$ . Therefore, we conclude that the precipitation with antisolvent followed by the annealing process led to the mixed-valent vanadium species present in  $Zn_4V_2O_9$ . Can you estimate the ratio  $V^{4+}/V^{5+}$ ?

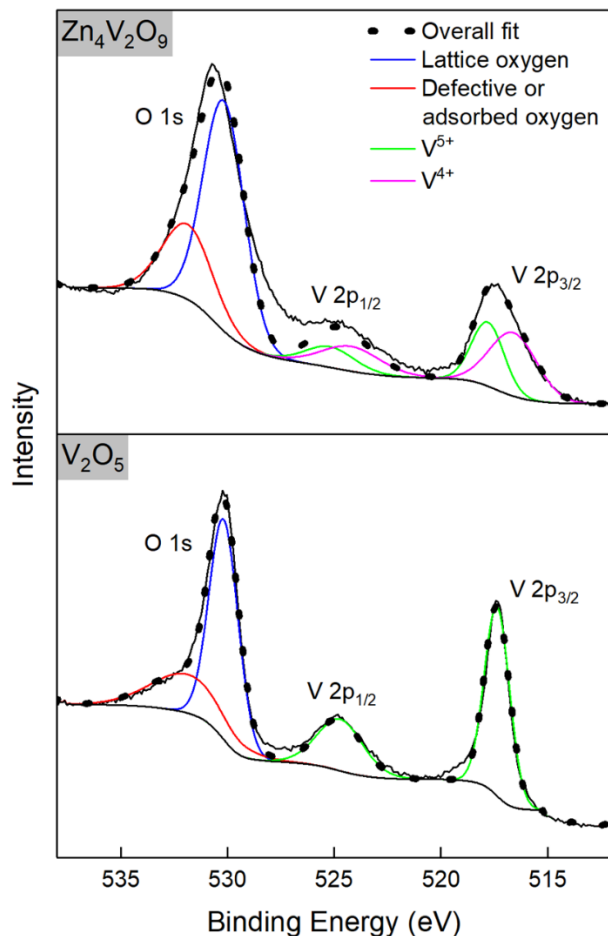


Figure 9. XPS data of the O 1s and V 2p regions from  $Zn_4V_2O_9$  (top) and a reference  $V_2O_5$  (bottom).

The optical property of  $Zn_4V_2O_9$  is evaluated by using diffuse reflectance UV–vis spectroscopy at room temperature (Figure 10a). The absorption edge is observed at  $\sim 428$  nm with the indirect band gap of 2.94 eV determined from a Tauc plot. In addition, a broad optical absorption is observed in the range of 2.25 – 2.94 eV suggesting that excitation of defect states is available in the sub-band gap region.<sup>87</sup> From the XPS analysis, we confirmed that the missing oxide anions create reduced vanadium species ( $V^{4+}$ ) in  $Zn_4V_2O_9$  prepared by the precipitation method. Furthermore,  $V^{4+}$  in the oxygen-vacancies-containing  $ZnV_2O_6$  and

$\text{Zn}_2\text{V}_2\text{O}_7$  gave rise to the additional states in between the valence and conduction band according to the previous reports.<sup>23,24</sup> Consequently, we conclude that the absorption tail originates from the  $\text{V}^{4+}$  mid-gap states.

We calculated the electronic structure of  $\text{Zn}_4\text{V}_2\text{O}_9$  using the HSE06 hybrid functional (Figure 10 b-c). Based on the band structure, a band gap of 3.93 eV is obtained. The  $\approx 1.0$  eV difference in the calculated and experimental band gaps is surprising given the accuracy of HSE06 with insulating systems. Nevertheless, the band structure calculation also reveals an indirect bandgap which is consistent with experiment. The conduction band is primarily composed of empty V 3d states with a minor contribution of empty Zn 4s states. On the other hand, the O 2p states are the dominant in the valence band with some contribution from the completely filled Zn 3d orbitals.

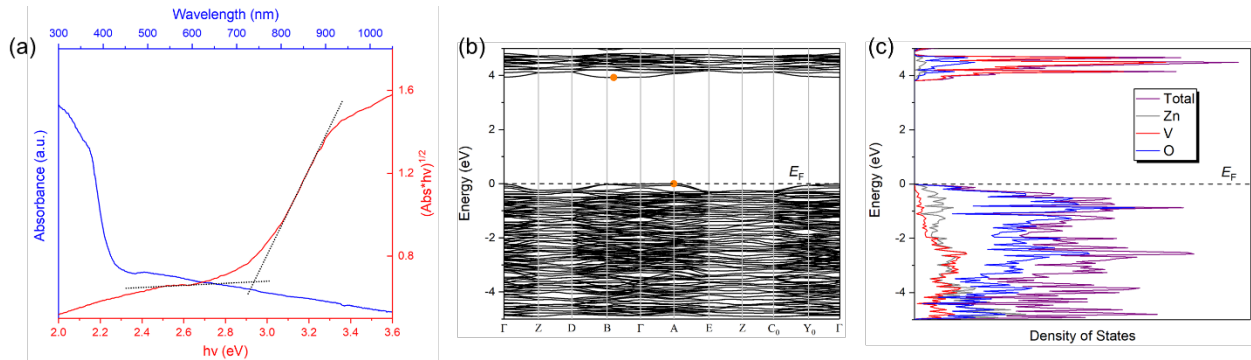


Figure 10. UV-vis spectrum plotted with a corresponding Tauc plot (a) of  $\text{Zn}_4\text{V}_2\text{O}_9$ . Band structure (b) and projected total density of states (b) calculated for the same compound.

According to the combinatorial library made by Mordkovich et al., the intensity of yellow luminescence (560 nm) varied depending on vanadium concentration in  $\text{ZnO}:\text{V}_2\text{O}_5$  system.<sup>36</sup> The samples in the concentration range of 32–40 % V exhibited a high luminescence efficiency with the maximum value obtained at 33 % V.<sup>36</sup> When the luminescence dependency on chemical composition was compared with the phase diagram of the  $\text{ZnO}-\text{V}_2\text{O}_5$  system, the yellow emission reached the maximum intensity in the area where  $\text{Zn}_4\text{V}_2\text{O}_9$  (33 % V) and  $\text{Zn}_3\text{V}_2\text{O}_8$  (40 % V) coexisted.<sup>36</sup> Although the finding was based on the low crystallinity samples, later reports further proved that  $\text{Zn}_3\text{V}_2\text{O}_8$  possesses a promising yellow luminescence property with the quantum yield of 43.6 % and quantum efficiency of 52 %.<sup>32,33,35</sup> Inspired by the previous work, we performed photoluminescence (PL) measurement for the as-synthesized  $\text{Zn}_4\text{V}_2\text{O}_9$  with excitation wavelengths of 310 and 320 nm. Despite the incident photon energy was sufficient to excite the oxide phase, there was no discernable emission observed. In general, the origin of zinc vanadate phosphors' luminescence is the one-electron charge transfer (CT) from O 2p orbital to vacant 3d orbital of  $\text{V}^{5+}$  in  $\text{VO}_4$  tetrahedra with  $T_d$  symmetry.<sup>33</sup> The significantly different luminescence quantum efficiencies — 0.09 %

and 52 % for  $\text{Zn}_2\text{V}_2\text{O}_7$  and  $\text{Zn}_3\text{V}_2\text{O}_8$ , respectively — were attributed to the different metal interactions stemming from their crystal structures.<sup>33</sup> Unlike the dimerized  $\text{VO}_4$  of  $\text{Zn}_2\text{V}_2\text{O}_7$ , the isolated vanadium oxide tetrahedra in  $\text{Zn}_3\text{V}_2\text{O}_8$  is responsible for a strong interaction between the adjacent V cations and weak interaction between Zn and V cations, providing the enhancement in the exciton diffusion lifetime.<sup>33</sup> Importantly,  $\text{Zn}_4\text{V}_2\text{O}_9$  also consists of isolated  $\text{VO}_4$  tetrahedra, leading us to predict a strong yellow emission. However, the reduced vanadium species ( $\text{V}^{4+}$ ) created by oxygen vacancies, as shown in the XPS data, possibly diminish the CT transition.

Next, we employ surface photovoltage spectroscopy (SPS) to characterize the ability of  $\text{Zn}_4\text{V}_2\text{O}_9$  to generate and separate charge carriers under illumination. In SPS a vibrating Kelvin probe measures the contact potential difference (CPD) of a material.<sup>88-90</sup> The CPD change under illumination corresponds to a surface photovoltage. The data for the  $\text{Zn}_4\text{V}_2\text{O}_9$  particle film on a FTO substrate is shown in Figure 11. The negative photovoltage is attributed to injection of photogenerated electrons in  $\text{Zn}_4\text{V}_2\text{O}_9$  into the FTO substrate, as shown in the insert. On this basis, the material is n-type. Using the tangent line for the major photovoltage feature, the compound has a 2.95 eV band gap, similar to the optical band gap of the material. However, the weak photovoltage signal at 2.25-2.95 eV suggests the presence of sub-band gap states. These states likely correspond to the  $\text{V}^{4+}$  ions that are also responsible for the visible absorption tail in the optical spectra. The sub-bandgap signal is much more pronounced than for  $\text{ZnV}_2\text{O}_6$  (ref 24) or  $\text{Zn}_2\text{V}_2\text{O}_7$  (ref 23), which indicates that  $\text{Zn}_4\text{V}_2\text{O}_9$  has a higher  $\text{V}^{4+}$  concentration. This is consistent with the XPS data.

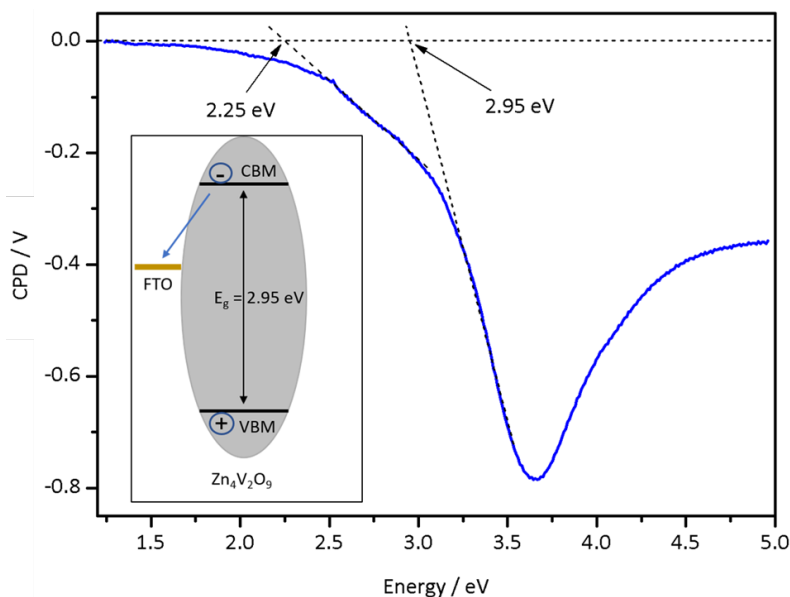


Figure 11. Surface photovoltage data of a  $\text{Zn}_4\text{V}_2\text{O}_9$  particle film on FTO. Inset: charge transfer causing the photovoltage signal.

To determine if  $\text{Zn}_4\text{V}_2\text{O}_9$  is able to facilitate photoelectrochemical reactions, linear sweep voltammograms under chopped simulated sunlight (from a 300 W Xe arc lamp) were performed on  $\text{Zn}_4\text{V}_2\text{O}_9$  coated FTO electrodes in degassed aqueous 0.1 M  $\text{Na}_2\text{SO}_4$  with 20% (v:v) added methanol or in aqueous 0.1 M  $\text{K}_2\text{SO}_4$ . Weak photocurrents were observed when the applied potentials exceeded +0.15 V vs NHE in aqueous methanol and + 0.6 V vs NHE in aqueous 0.1 M  $\text{K}_2\text{SO}_4$ . In the latter electrolyte, the current is attributed to water oxidation, although no  $\text{O}_2$  could be detected at this low activity. Based on the photoonset potential in aqueous methanol, the Fermi level in  $\text{Zn}_4\text{V}_2\text{O}_9$  is at +0.15 V vs NHE (0.56 V RHE). Overall,  $\text{Zn}_4\text{V}_2\text{O}_9$  is ten times less photoactive than the  $\text{ZnV}_2\text{O}_6$  phase for which methanol oxidation photocurrents of  $20 \mu\text{A}\cdot\text{cm}^{-2}$  at 1.6 V vs RHE were observed under  $150 \text{ mW}\cdot\text{cm}^{-2}$  visible light illumination.<sup>24</sup> The lower activity of  $\text{Zn}_4\text{V}_2\text{O}_9$  is attributed to the high concentration of  $\text{V}^{4+}$  sub band gap states, which promote recombination with the photogenerated holes. A similar role of reduced  $\text{Ti}^{3+}$  sites had been observed previously for  $\text{SrTiO}_3$  Zhao, Z., R.V. Goncalves, S.K. Barman, E.J. Willard, E. Byle, R. Perry, Z. Wu, M.N. Huda, A.J. Moulé, and F.E. Osterloh, *Electronic structure basis for enhanced overall water splitting photocatalysis with aluminum doped SrTiO3 in natural sunlight*. Energy & Environmental Science, 2019. 12: p. 1385-1395. <https://doi.org/10.1039/C9EE00310J> and for  $\text{Fe}^{2+}$  states in hematite. Lohaus, C., A. Klein, and W. Jaegermann, Limitation of Fermi level shifts by polaron defect states in hematite photoelectrodes. Nature Communications, 2018. 9(1): p. 4309. <https://doi.org/10.1038/s41467-018-06838-2>

It is also worth comparing the structure–PEC property relationship of two zinc-rich vanadates  $\text{Zn}_3\text{V}_2\text{O}_8$  and  $\text{Zn}_4\text{V}_2\text{O}_9$ . With  $\text{ZnO}_x$  ( $x = 4, 5, \text{ and } 6$ ) coordination polyhedra, both compounds have a layered crystal structure.<sup>53,54</sup> Contribution of empty Zn 4s orbitals as well as V 3d states to the conduction band is another feature that two compounds have in common.<sup>93</sup> However, the  $\text{Zn}_3\text{V}_2\text{O}_8$  has an increased density of states as well as valence band width in the valence band due to significant contribution of Zn 3d states in addition to O 2p states.<sup>93</sup> In contrast, the involvement of Zn 3d states in the valence band of  $\text{Zn}_4\text{V}_2\text{O}_9$  is limited. Even the oxygen vacancy unlikely improves the Zn 3d states' contribution because only vanadium cations become reduced for the charge balance. Considering the impact of p-d orbital hybridization between  $\text{O}^{2-}$  and  $d^{10}$  metal ions to band gap, band edges, and band width of metal oxides,<sup>93-96</sup> the poor PEC property of  $\text{Zn}_4\text{V}_2\text{O}_9$  is attributed to low mobility of photoexcited holes in the valence band.

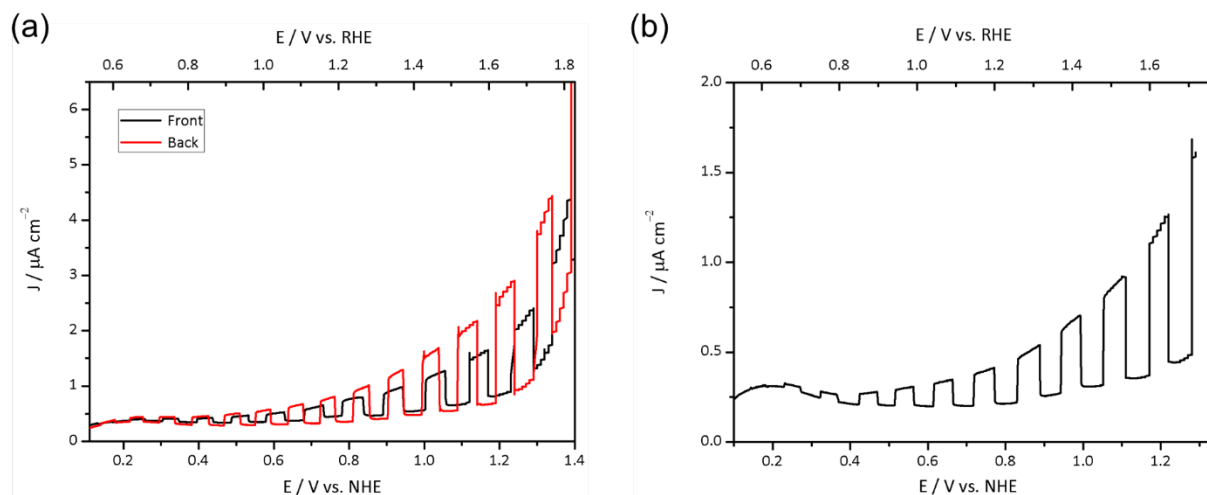


Figure 12. Photoelectrochemical scans of  $\text{Zn}_4\text{V}_2\text{O}_9$  on FTO with intermitted illumination from Xe lamp ( $100 \text{ mW} \cdot \text{cm}^{-2}$ ). The electrolytes are (a) degassed aqueous  $0.1 \text{ M Na}_2\text{SO}_4$  (pH 7) containing 20 % (v/v) methanol, or, (b)  $0.1 \text{ M K}_2\text{SO}_4$  aqueous solution (pH 7).

## Conclusion

In-depth study of a deep eutectic solvent (DES)-involved precipitation route was conducted within the  $\text{ZnO}$ - $\text{V}_2\text{O}_5$  system. The ternary phase  $\text{Zn}_3(\text{OH})_2\text{V}_2\text{O}_7 \cdot n\text{H}_2\text{O}$  together with  $\text{Zn}_5(\text{OH})_6(\text{CO}_3)_2$  were obtained simply upon addition of antisolvent DI  $\text{H}_2\text{O}$  to the precursor solution. We determined the synthetic parameters to control size/morphology of the precipitate, i.e., temperature of the antisolvent and its addition rate. The low temperature antisolvent causes a lateral growth of individual 2D nanosheets ranging up to  $\sim 2 \mu\text{m}$ . The formation mechanism of a unique flower-like agglomerate is identified by the slow antisolvent addition rate. It is revealed that the layered structure of  $\text{Zn}_3(\text{OH})_2\text{V}_2\text{O}_7 \cdot n\text{H}_2\text{O}$  can host extra molecular species as well as various amount of  $\text{H}_2\text{O}$  depending on the synthetic conditions. Two zinc-rich vanadium oxides  $\text{ZnO}/\text{Zn}_3\text{V}_2\text{O}_8$  and  $\text{Zn}_4\text{V}_2\text{O}_9$  are prepared by a heat treatment of the precipitates. The phase evolution is understood by the similarity in crystal structures of zinc hydroxy vanadate hydrate and zinc-rich vanadates. The outstanding improvement of solid-state diffusion between  $\text{ZnO}$  and  $\text{Zn}_3\text{V}_2\text{O}_8$  was achieved by their intimate mixing, producing the metastable  $\text{Zn}_4\text{V}_2\text{O}_9$  within 30 seconds of annealing. We confirmed that the bond stretching mode of  $[\text{VO}_4]^{3-}$  in the Raman spectrum of  $\text{Zn}_4\text{V}_2\text{O}_9$  is split in the wavenumber range of  $748 - 952 \text{ cm}^{-1}$  due to the four cryptographically independent vanadium sites. The most zinc-rich vanadate exhibits an indirect optical band gap of  $2.94 \text{ eV}$  with the absorption tail in  $2.25 - 2.94 \text{ eV}$ , which is ascribed to  $\text{V}^{4+}$  ions created by oxygen vacancies. Surface photovoltage spectra confirm the  $2.95 \text{ eV}$  band gap and suggest n-type character for  $\text{Zn}_4\text{V}_2\text{O}_9$ , based on the negative photovoltage signal. The photoluminescence experiment on  $\text{Zn}_4\text{V}_2\text{O}_9$  reveals that the reduced vanadium cation acts as an inhibitor in yellow emission by decreasing an electron charge transfer in the  $\text{VO}_4$  tetrahedra. Photoelectrochemical (PEC) experiments

reveal some activity of the vanadate for water and methanol oxidation, when the applied potential is over 0.6 V and 0.15 V vs NHE, respectively. However, the photocurrents are small, and limited by the high concentration of  $V^{4+}$  defects, which function as electron-hole recombination sites. Overall, this work demonstrates versatility of DES as a reaction medium in preparation of semiconducting ternary metal oxides and potentially enables other metastable oxides attainable.

### Acknowledgements

We thank Dr. Kirill Kovnir and Dr. Javier Vela (Department of Chemistry, Iowa State University, and Ames Laboratory) for the access to the PXRD diffractometer and the UV–vis spectrometer, respectively; Dr. Warren Straszheim (Materials Analysis Research Laboratory, Iowa State University) for the help with SEM/EDS measurement; Dr. Dapeng Jing (Materials Analysis Research Laboratory, Iowa State University) for the assistance with XPS data acquisition; Dr. Brett Boote (Chemical Instrument Services, Department of Chemistry, Iowa State University) for fruitful discussions; Dr. Wenqian Xu and Dr. Andrey Yakovenko at 17-BM beamline, APS ANL, and Dr. Volodymyr Gvozdetzkyi, Dr. Colin Harmer, and Gourab Bhaskar at Iowa State University for assistance in HT-PXRD experiments. The financial support from the Iowa State University is gratefully acknowledged. Use of the Advanced Photon Source at Argonne National Laboratory was supported by the U.S. Department of Energy, Office of Science, Office of Basic Energy Sciences, under Contract No. DE-AC02-06CH11357. Support for surface photovoltage spectroscopy measurements was provided by the U.S. Department of Energy, Office of Science, Office of Basic Energy Sciences under Award Number DOE-SC0015329.

### References

1. Kirklin, S.; Saal, J. E.; Meredig, B.; Thompson, A.; Doak, J. W.; Aykol, M.; Rühl, S.; Wolverton, C. The Open Quantum Materials Database (OQMD): assessing the accuracy of DFT formation energies. *Npj Comput. Mater.* **2015**, 1, 15010.
2. Bergerhoff, G.; Hundt, R.; Sievers, R.; Brown, I. D. The inorganic crystal structure data base. *J. Chem. Inf. Model.* **1983**, 23, 66–69.
3. F. Karlsruhe, Inorganic Crystal Structure Database, <http://icsd.fiz-karlsruhe.de/icsd/>
4. Lotfi, S.; Brgoch, J. Discovering Intermetallics Through Synthesis, Computation, and Data-Driven Analysis. *Chem. Eur. J.* **2020**, 26, 8689–8697.

5. Aykol, M.; Dwaraknath, S. S.; Sun, W.; Persson, K. A. Thermodynamic limit for synthesis of metastable inorganic materials. *Sci. Adv.* **2018**, 4, eaaq0148.
6. Bartel, C. J.; Millican, S. L.; Deml, A. M.; Rumpitz, J. R.; Tumas, W.; Weimer, A. W.; Lany, S.; Stevanovic, V.; Musgrave, C. B.; Holder, A. M. Physical descriptor for the Gibbs energy of inorganic crystalline solids and temperature-dependent materials chemistry. *Nat. Commun.* **2018**, 9, 4168.
7. Montanari, E.; Righi, L.; Calestani, G.; Migliori, A.; Gilioli, E.; Bolzoni, F. *Chem. Mater.* **2005**, 17, 7, 1765–1773.
8. Omata, T.; Nagatani, H.; Suzuki, I.; Kita, M.; Yanagi, H.; Ohashi, N. Wurtzite CuGaO<sub>2</sub>: A New Direct and Narrow Band Gap Oxide Semiconductor Applicable as a Solar Cell Absorber. *J. Am. Chem. Soc.* **2014**, 136, 3378–3381.
9. Nagatani, H.; Suzuki, I.; Kita, M.; Tanaka, M.; Katsuya, Y.; Sakata, O.; Miyoshi, S.; Yamaguchi, S.; Omata, T. Structural and Thermal Properties of Ternary Narrow-Gap Oxide Semiconductor; Wurtzite-Derived  $\beta$ -CuGaO<sub>2</sub>. *Inorg. Chem.* **2015**, 54, 1698–1704.
10. Cheng, H.; Huang, B.; Dai, Y.; Qin, X.; Zhang, X.; Wang, Z.; Jiang, M. Visible-light photocatalytic activity of the metastable Bi<sub>20</sub>TiO<sub>32</sub> synthesized by a high-temperature quenching method. *J. Solid State Chem.* **2009**, 182, 2274–2278.
11. Song, J.; Ni, X.; Gao, L.; Zheng, H. Synthesis of metastable h-MoO<sub>3</sub> by simple chemical precipitation. *Mater. Chem. Phys.* **2007**, 102, 245–248.
12. Bose, A. C.; Ramamoorthy, R.; Ramasamy, S. Formability of metastable tetragonal solid solution in nanocrystalline NiO–ZrO powders. *Mater. Lett.* **2000**, 44, 203–207.
13. Ahn, T.; Kim, J. H.; Yang, H.-M.; Lee, J. W.; Kim, J.-D. Formation Pathways of Magnetite Nanoparticles by Coprecipitation Method. *J. Phys. Chem. C* **2012**, 116, 6069–6076.
14. Abellán, G.; Coronado, E.; Martí-Gastaldo, C.; Ribera, A.; Sánchez-Royo, J. F. Layered double hydroxide (LDH)–organic hybrids as precursors for low-temperature chemical synthesis of carbon nanoforms. *Chem. Sci.* **2012**, 3, 1481–1485.

15. Lenders, J. J. M.; Mirabello, G.; Sommerdijk, N. A. J. M. Bioinspired magnetite synthesis *via* solid precursor phases. *Chem. Sci.* **2016**, 7, 5624–5634.
16. Abbott, A. P.; Boothby, D.; Capper, G.; Davies, D. L.; Rasheed, R. K. Deep Eutectic Solvents Formed between Choline Chloride and Carboxylic Acids: Versatile Alternatives to Ionic Liquids. *J. Am. Chem. Soc.* **2004**, 126, 9142–9147.
17. Smith, E. L.; Abbott, A. P.; Ryder, K. S. Deep Eutectic Solvents (DESs) and Their Applications. *Chem. Rev.* **2014**, 114, 11060–11082.
18. Ciocirlan, O.; Iulian, O.; Croitoru, O. Effect of Temperature on the Physico-chemical Properties of Three Ionic Liquids Containing Choline Chloride. *Rev. Chim.* **2010**, 61, 721–723.
19. Hansen, B. B.; Spittle, S.; Chen, B.; Poe, D.; Zhang, Y.; Klein, J. M.; Horton, A.; Adhikari, L.; Zelovich, T.; Doherty, B. W.; Gurkan, B.; Maginn, E. J.; Ragauskas, A.; Dadmun, M.; Zawodzinski, T. A.; Baker, G. A.; Tuckerman, M. E.; Savinell, R. F.; Sangoro, J. R. Deep Eutectic Solvents: A Review of Fundamentals and Applications. *Chem. Rev.* **2021**, 121, 1232–1285.
20. Boston, R.; Foeller, P. Y.; Sinclair, D. C.; Reaney, I. M. Synthesis of Barium Titanate Using Deep Eutectic Solvents. *Inorg. Chem.* **2017**, 56, 542–547.
21. Söldner, A.; Zach, J.; Iwanow, M.; Gartner, T.; Schlosser, M.; Pfitzner, A.; König, B. Preparation of Magnesium, Cobalt and Nickel Ferrite Nanoparticles from Metal Oxides using Deep Eutectic Solvents. *Chem. Eur. J.* **2016**, 22, 13108–13113.
22. Thorat, G. M.; Jadhav, H. S.; Roy, A.; Chung, W.-J.; Seo, J. G. Dual Role of Deep Eutectic Solvent as a Solvent and Template for the Synthesis of Octahedral Cobalt Vanadate for an Oxygen Evolution Reaction. *ACS Sustain. Chem. Eng.* **2018**, 6 (12), 16255–16266.
23. Hong, S.; Doughty, R. M.; Osterloh, F. E.; Zaikina, J. V. Deep eutectic solvent route synthesis of zinc and copper vanadate n-type semiconductors - mapping oxygen vacancies and their effect on photovoltage. *J. Mater. Chem. A* **2019**, 7, 12303–12316.
24. Hong, A.; Burkhov, S. J.; Doughty, R. M.; Cheng, Y.; Ryan, B. J.; Mantravadi, A.; Roling, L. T.; Panthani, M. G.; Osterloh, F. E.; Smith, E. A.; Zaikina, J. V. Local Structural Disorder in

- Metavanadates  $MV_2O_6$  ( $M = \text{Zn}$  and  $\text{Cu}$ ) Synthesized by the Deep Eutectic Solvent Route: Photoactive Oxides with Oxygen Vacancies. *Chem. Mater.* **2021**, 33, 1667–1682.
25. Baby, J. N.; Sriram, B.; Wang, S. -F.; George, M. Effect of Various Deep Eutectic Solvents on the Sustainable Synthesis of  $\text{MgFe}_2\text{O}_4$  Nanoparticles for Simultaneous Electrochemical Determination of Nitrofurantoin and 4-Nitrophenol. *ACS Sustain. Chem. Eng.* **2020**, 8, 1479–1486.
  26. Datta, S.; Jo, C.; De Volder, M.; Torrente-Murciano, L. Morphological Control of Nanostructured  $\text{V}_2\text{O}_5$  by Deep Eutectic Solvents. *ACS Appl. Mater. Interfaces* **2020**, 12, 18803–18812.
  27. Baby, J. N.; Sriram, B.; Wang, S. -F.; George, M.; Govindasamy, M.; Joseph, X. B. Deep eutectic solvent-based manganese molybdate nanosheets for sensitive and simultaneous detection of human lethal compounds: comparing the electrochemical performances of M-molybdate ( $M = \text{Mg}$ ,  $\text{Fe}$ , and  $\text{Mn}$ ) electrocatalysts. *Nanoscale* **2020**, 12, 19719.
  28. Dong, J. -Y.; Hsu, Y. -J.; Wong, D. S. -H.; Lu, S. -Y. Growth of ZnO Nanostructures with Controllable Morphology Using a Facile Green Antisolvent Method. *J. Phys. Chem. C* **2010**, 114, 8867–8872.
  29. Dong, J. -Y.; Lin, W. -H.; Hsu, Y. -J.; Wong, D. S. -H.; Lu, S. -Y. Ultrafast formation of ZnO mesocrystals with excellent photocatalytic activities by a facile Tris-assisted antisolvent process. *CrystEngComm* **2011**, 13, 6218.
  30. Dong, J. -Y.; Lin, C. -H.; Hsu, Y. -J.; Lu, S. -Y.; Wong, D. S. -H. Single-crystalline mesoporous ZnO nanosheets prepared with a green antisolvent method exhibiting excellent photocatalytic efficiencies. *CrystEngComm* **2012**, 14, 4732–4737.
  31. Lu, Y. -H.; Lin, W. -H.; Yang, C. -Y.; Chiu, Y. -H.; Pu, Y. -C.; Lee, M. -H.; Tseng, Y. -C.; Hsu, Y. -J. A facile green antisolvent approach to  $\text{Cu}^{2+}$ -doped ZnO nanocrystals with visible-light-responsive photoactivities. *Nanoscale* **2014**, 6, 8796.
  32. Nakajima, T.; Isobe, M.; Tsuchiya, T.; Ueda, Y.; Kumagai, T. A revisit of photoluminescence property for vanadate oxides  $\text{AVO}_3$  ( $A: \text{K}$ ,  $\text{Rb}$  and  $\text{Cs}$ ) and  $\text{M}_3\text{V}_2\text{O}_8$  ( $M: \text{Mg}$  and  $\text{Zn}$ ). *J. Lumin.* **2009**, 129, 1598–1601.

33. Nakajima, T.; Isobe, M.; Tsuchiya, T.; Ueda, Y.; Manabe, T. Correlation between Luminescence Quantum Efficiency and Structural Properties of Vanadate Phosphors with Chained, Dimerized, and Isolated VO<sub>4</sub> Tetrahedra. *J. Phys. Chem. C* **2010**, 114, 5160–5167.
34. Dang, P.; Liu, D.; Wei, Y.; Li, G.; Lian, H.; Shang, M.; Lin, J. Highly Efficient Cyan-Green Emission in Self-Activated Rb<sub>3</sub>RV<sub>2</sub>O<sub>8</sub> (R = Y, Lu) Vanadate Phosphors for Full-Spectrum White Light-Emitting Diodes (LEDs). *Inorg. Chem.* **2020**, 59, 6026–6038.
35. Qian, T.; Fan, B.; Wang, H.; Zhu, S. Structure and luminescence properties of Zn<sub>3</sub>V<sub>2</sub>O<sub>8</sub> yellow phosphor for white light emitting diodes. *Chem. Phys. Lett.* **2019**, 715, 34–39.
36. Mordkovich, V. Z.; Hayashi, H.; Haemori, M.; Fukumura, T.; Kawasaki, M. Discovery and Optimization of New ZnO-Based Phosphors Using a Combinatorial Method. *Adv. Funct. Mater.* **2003**, 13, 519–524.
37. Kudo, A.; Omori, K.; Kato, H. A Novel Aqueous Process for Preparation of Crystal Form-Controlled and Highly Crystalline BiVO<sub>4</sub> Powder from Layered Vanadates at Room Temperature and Its Photocatalytic and Photophysical Properties. *J. Am. Chem. Soc.* **1999**, 121, 11459–11467.
38. Yan, Q.; Li, G.; Newhouse, P. F.; Yu, J.; Persson, K. A.; Gregoire, J. M.; Neaton, J. B. Mn<sub>2</sub>V<sub>2</sub>O<sub>7</sub>: An Earth Abundant Light Absorber for Solar Water Splitting. *Adv. Energy Mater.* **2015**, 5, 1401840.
39. Zhang, J.; Wang, T.; Chang, X.; Li, A.; Gong, J. Fabrication of porous nanoflake BiMO<sub>x</sub> (M = W, V, and Mo) photoanodes *via* hydrothermal anion exchange. *Chem. Sci.* **2016**, 7, 6381–6386.
40. PDXL: Integrated X-ray powder diffraction software, Version 2.8.1.1; Rigaku: 2018.
41. Chupas, P. J.; Chapman, K. W.; Kurtz, C.; Hanson, J. C.; Lee, P. L.; Grey, C. P. A versatile sample-environment cell for non-ambient X-ray scattering experiments. *J. Appl. Crystallogr.* **2008**, 41, 822–824.
42. Toby, B. H.; Von Dreele, R. B. GSAS-II: the genesis of a modern open-source all purpose crystallography software package. *J. Appl. Crystallogr.* **2013**, 46, 544–549.
43. Kresse, G.; Furthmüller, J., Efficient iterative schemes for ab initio total-energy calculations using a plane-wave basis set. *Phys. Rev. B: Condens. Matter Mater. Phys.* **1996**, 54 (16), 11169–11186.

44. Blöchl, P. E., Projector augmented-wave method. *Phys. Rev. B: Condens. Matter Mater. Phys.* **1994**, 50 (24), 17953-17979.
45. Heyd, J.; Scuseria, G. E.; Ernzerhof, M., Hybrid functionals based on a screened Coulomb potential. *J. Chem. Phys.* **2003**, 118 (18), 8207-8215.
46. Monkhorst, H. J.; Pack, J. D., Special points for Brillouin-zone integrations. *Phys. Rev. B: Condens. Matter Mater. Phys.* **1976**, 13 (12), 5188-5192.
47. Parlinski, K.; Li, Z. Q.; Kawazoe, Y., First-principles determination of the soft mode in cubic ZrO<sub>2</sub>. *Phys. Rev. Lett.* **1997**, 78 (21), 4063-4066.
48. Fonari, A.; Stauffer, S. Vasp\_raman.Py. 2013. <https://github.com/raman-sc/VASP/>.
49. Kodera, M., J. Wang, B.A. Nail, J. Liu, H. Urabe, T. Hisatomi, M. Katayama, T. Minegishi, F.E. Osterloh, and K. Domen, Investigation of charge separation in particulate oxysulfide and oxynitride photoelectrodes by surface photovoltage spectroscopy. *Chem. Phys. Lett.* **2017**, 683, 140-144.
50. Zavalij, P. Y.; Zhang, F.; Whittingham, M. S. A New Zinc Pyrovanadate, Zn<sub>3</sub>(OH)<sub>2</sub>V<sub>2</sub>O<sub>7</sub>·2H<sub>2</sub>O, from X-ray Powder Data. *Acta Cryst.* **1997**, C53, 1738–1739.
51. Chirayil, T.; Zavalij, P. Y.; Whittingham, M. S. Hydrothermal Synthesis of Vanadium Oxides, *Chem. Mater.* **1998**, 10, 2629–2640.
52. Zavalij, P. Y.; Zhang, F.; Whittingham, M. S. The zinc–vanadium–oxygen–water system: hydrothermal synthesis and characterization. *Solid State Sci.* **2002**, 4, 591–597.
53. Gopal, R.; Calvo, C. Crystal Structure of α-Zn<sub>3</sub>(VO<sub>4</sub>)<sub>2</sub>, *Can. J. Chem.* **1971**, 49, 3056–3059.
54. Waburg, M.; Müller-Buschbaum, H. Ein neues metastabiles Zinkoxovanadat: Zn<sub>4</sub>V<sub>2</sub>O<sub>9</sub>. *Monatsh. Chem.* **1986**, 117, 131–138.
55. Abbott, A. P.; Capper, G.; Davies, D. L.; McKenzie, K. J.; Obi, S. U. Solubility of Metal Oxides in Deep Eutectic Solvents Based on Choline Chloride. *J. Chem. Eng. Data* **2006**, 51, 1280–1282.
56. Nagy, Z. K.; Fujiwara, M.; Woo, X. Y.; Braatz, R. D. Determination of the Kinetic Parameters for the Crystallization of Paracetamol from Water Using Metastable Zone Width Experiments. *Ind. Eng. Chem. Res.* **2008**, 47, 1245–1252.

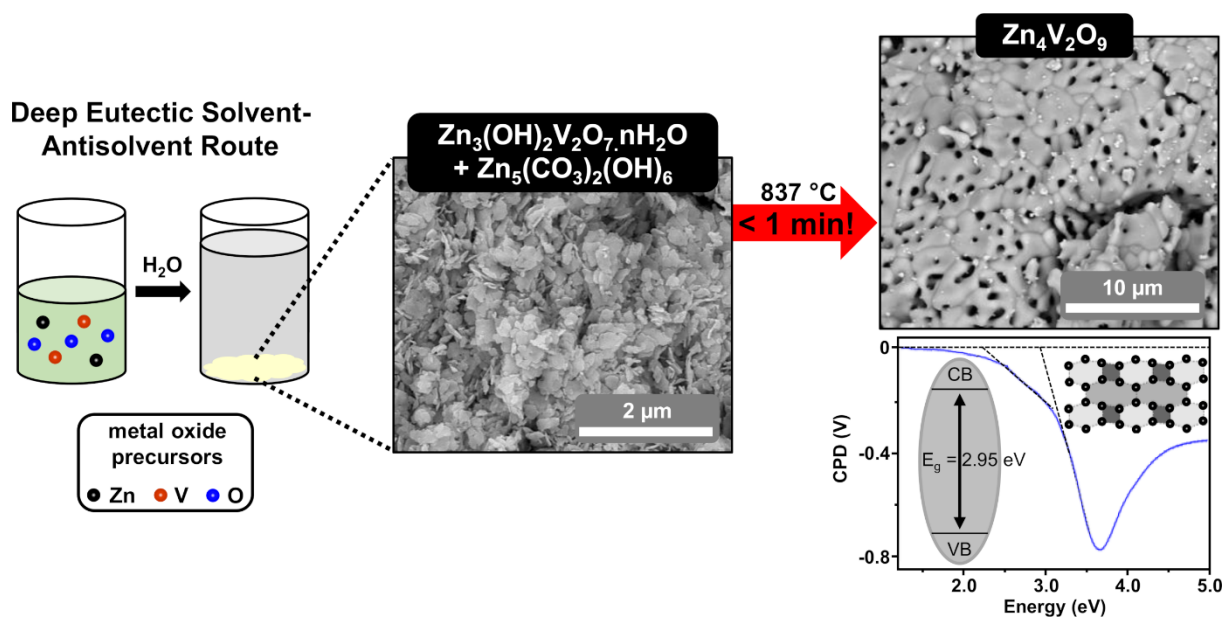
57. Kim, K. J.; Mersmann, A. Estimation of metastable zone width in different nucleation processes. *Chem. Eng. Sci.* **2001**, *56*, 2315–2324.
58. Sangwal, K. A novel self-consistent Nyvlt-like equation for metastable zone width determined by the polythermal method. *Cryst. Res. Technol.* **2009**, *44*, 231–247.
59. Laird, A.; Chougule, M.; Hamad, M.; Morris, K. Thermodynamics Associated with Monitoring Pre-nucleation Aggregation at High Supersaturation. *Int. J. Pharm. Sci. Rev. Res.* **2013**, *18*, 6–12.
60. Clark, M. D.; Morris, K. R.; Tomassone, M. S. Correlation of Solubility with the Metastable Limit of Nucleation Using Gauge-Cell Monte Carlo Simulations. *Langmuir* **2017**, *33*, 9081–9090.
61. Yu, Y.; Niu, C.; Han, C.; Zhao, K.; Meng, J.; Xu, X.; Zhang, P.; Wang, L.; Wu, Y.; Mai, L. Zinc Pyrovanadate Nanoplates Embedded in Graphene Networks with Enhanced Electrochemical Performance. *Ind. Eng. Chem. Res.* **2016**, *55*, 2992–2999.
62. Shi, R.; Wang, Y.; Zhou, F.; Zhu, Y.  $Zn_3V_2O_7(OH)_2(H_2O)_2$  and  $Zn_3V_2O_8$  nanostructures: controlled fabrication and photocatalytic performance. *J. Mater. Chem.*, **2011**, *21*, 6313–6320.
63. Gan, L. -H.; Deng, D.; Zhang, Y.; Li, G.; Wang, X.; Jiang, L.; Wang, C. -R.  $Zn_3V_2O_8$  hexagon nanosheets: a high-performance anode material for lithium-ion batteries. *J. Mater. Chem. A* **2014**, *2*, 2461–2466.
64. Xia, C.; Guo, J.; Lei, Y.; Liang, H.; Zhao, C.; Alshareef, H. N. Rechargeable Aqueous Zinc-Ion Battery Based on Porous Framework Zinc Pyrovanadate Intercalation Cathode. *Adv. Mater.* **2018**, *30*, 1705580.
65. Li, Y.; Teng, Y.; Zhang, Z.; Feng, Y.; Xue, P.; Tong, W.; Liu, X. Microwave-assisted synthesis of novel nanostructured  $Zn_3(OH)_2V_2O_7 \cdot 2H_2O$  and  $Zn_2V_2O_7$  as electrode materials for supercapacitors. *New J. Chem.*, **2017**, *41*, 15298–15304.
66. Iablokov, V.; Beaumont, S. K.; Alayoglu, S.; Pushkarev, V. V.; Specht, C.; Gao, J.; Alivisatos, A. P.; Kruse, N.; Somorjai, G. A. Size-Controlled Model Co Nanoparticle Catalysts for  $CO_2$  Hydrogenation: Synthesis, Characterization, and Catalytic Reactions. *Nano Lett.* **2012**, *12*, 3091–3096.
67. Yao, Y. F. Y.; Kummer, J. T. Ion exchange properties of and rates of ionic diffusion in beta-alumina. *J. Inorg. Nucl. Chem.* **1967**, *29*, 2453.

68. Chowdhury, M. T.; Takekawa, R.; Iwai, Y.; Kuwata, N.; Kawamura J. Lithium ion diffusion in Li  $\beta$ -alumina single crystals measured by pulsed field gradient NMR spectroscopy. *J. Chem. Phys.* **2014**, 140, 124509.
69. Zhao, C.; Liu, L.; Qi, X.; Lu, Y.; Wu, F.; Zhao, J.; Yu, Y.; Hu, Y. -S.; Chen, L. Solid-State Sodium Batteries. *Adv. Energy Mater.* **2018**, 8, 1703012.
70. Shukla, A. K.;Ercius, P.; Gautam, A. R. S.; Cabana, J.; Dahmen, U. Electron Tomography Analysis of Reaction Path during Formation of Nanoporous NiO by Solid State Decomposition. *Cryst. Growth Des.* **2014**, 14, 2453–2459.
71. Dehmen, U.; Kim, M. G.; Searcy, A. W.; Microstructural evolution during the decomposition of Mg(OH)<sub>2</sub>. *Ultramicroscopy* **1987**, 23, 365–370.
72. Van Aken P. A.; Langenhorst, F. Nanocrystalline, porous periclase aggregates as product of brucite dehydration. *Eur. J. Mineral.* **2001**, 13, 329–341.
73. Kurzawa, M.; Rychlowska-Himmel, I.; Bosacka, M.; Blonska-Tabero, A. Reinvestigation of Phase Equilibria in the V<sub>2</sub>O<sub>5</sub>–ZnO System. *J. Therm. Anal. Calorim.* **2001**, 64, 1113–1119.
74. Sinhamahapatra, A.; Giri, A. K.; Pal, P.; Pahari, S. K.; Bajaj, H. C.; Panda, A. B. A rapid and green synthetic approach for hierarchically assembled porous ZnO nanoflakes with enhanced catalytic activity. *J. Mater. Chem.* **2012**, 22, 17227–17235.
75. Chen, X.; Chen, D.; Lv, P.; Yan, F.; Zhan, Z.; Li, B.; Huang, F.; Liang, J. Subsolidus phase relationships in the system ZnO–V<sub>2</sub>O<sub>5</sub>–WO<sub>3</sub> research on suitable flux for ZnO crystal growth. *J. Alloys Compd.* **2009**, 476, 241–244.
76. Rychlowska-Himmel, I.; Blonska-Tabero, A. Synthesis and Thermal Stability of Zn<sub>4</sub>V<sub>2</sub>O<sub>9</sub>. *J. Therm. Anal. Calorim.* **2001**, 64, 1121–1125.
77. Yang, L.; Tang, Y.; Tong, L.; Zhou, H.; Ding, J.; Fan, T.; Zhang, D. Efficient visible light photocatalytic water oxidation on Zn<sub>3</sub>(OH)<sub>2</sub>V<sub>2</sub>O<sub>7</sub>·2H<sub>2</sub>O nanoplates: Effects of exposed facet and local crystal structure distortion. *Appl. Surf. Sci.* **2015**, 346, 115–123.

78. Frost, R. L.; Palmer, S. J.; Čejka, J.; Sejkora, J.; Plášil, J.; Bahfenne, S.; Keeffe, E. C. A Raman spectroscopic study of the different vanadate groups in solid-state compounds – model case: mineral phases vésigniéite  $[\text{BaCu}_3(\text{VO}_4)_2(\text{OH})_2]$  and volborthite  $[\text{Cu}_3\text{V}_2\text{O}_7(\text{OH})_2 \cdot 2\text{H}_2\text{O}]$ . *J. Raman Spectrosc.* **2011**, 42, 1701–1710.
79. Hales, M. C.; Frost, R. L. Thermal Analysis of Smithsonite and Hydrozincite. *J. Therm. Anal. Calorim.* **2008**, 91, 855–860.
80. Zallen, R. The Physics of Amorphous Solids. Wiley, New York, **1983**.
81. Smith Jr, J. E.; Brodsky, M. H.; Crowder, B. L.; Nathan, M. I.; Pinczuk, A. Raman Spectra of Amorphous Si and Related Tetrahedrally Bonded Semiconductors. *Phys. Rev. Lett.* **1971**, 26, 642–646.
82. Ni, S.; Wang, X.; Zhou, G.; Yang, F.; Wang, J.; He, D. Crystallized  $\text{Zn}_3(\text{VO}_4)_2$ : Synthesis, characterization and optical property. *J. Alloys Compd.* **2010**, 491, 378–381.
83. Unnimaya, A. N.; Suresh, E. K.; Ratheesh, R. Crystal structure and microwave dielectric properties of new alkaline earth vanadate  $\text{A}_4\text{V}_2\text{O}_9$  (A = Ba, Sr, Ca, Mg and Zn) ceramics for LTCC applications. *Mater. Res. Bull.* **2017**, 88, 174–181.
84. Biesinger, M. C.; Lau, L. W. M.; Gerson, A. R.; Smart, R. S. C. Resolving surface chemical states in XPS analysis of first row transition metals, oxides and hydroxides: Sc, Ti, V, Cu and Zn. *Appl. Surf. Sci.* **2010**, 257, 887–898.
85. Biesinger, M. C.; Payne, B. P.; Lau, L. W. M.; Gerson, A.; Smart, R. S. C. X-ray photoelectron spectroscopic chemical state quantification of mixed nickel metal, oxide and hydroxide systems. *Surf. Interface Anal.* **2009**, 41, 324–332.
86. Silversmit, G., Depla, D., Poelman, H., Marin, G. B., De Gryse, R. An XPS study on the surface reduction of  $\text{V}_2\text{O}_5(001)$  induced by  $\text{Ar}^+$  ion bombardment. *Surf. Sci.*, **2006**, 600, 3512–3517.
87. Kröger, F. A.; Vink, H. J. Relations between the Concentrations of Imperfections in Crystalline Solids. *Solid State Phys.* **1956**, 3, 307–435.
88. Dittrich, T.; Fengler, S., Surface Photovoltage Analysis of Photoactive Materials. World Scientific Publishing Europe Ltd.: London, **2020**; p 287.

89. Kronik, L.; Shapira, Y., Surface Photovoltage Spectroscopy of Semiconductor Structures: At the Crossroads of Physics, Chemistry and Electrical Engineering. *Surf. Interface Anal.* **2001**, 31 (10), 954-965
90. Liqiang, J.; Xiaojun, S.; Jing, S.; Weimin, C.; Zili, X.; Yaoguo, D.; Honggang, F., Review of surface photovoltage spectra of nano-sized semiconductor and its applications in heterogeneous photocatalysis. *Sol. Energy Mater. Sol. Cells* **2003**, 79 (2), 133-151.
91. X. Ma, Z. Wu, E. J. Roberts, R. Han, G. Rao, Z. Zhao, M. Lamoth, X. Cui, R. D. Britt and F. E. Osterloh, *J. Phys. Chem. C* **2019**, 123, 25081-25090.
92. X. Ma, X. Cui, Z. Zhao, M. A. Melo, E. J. Roberts and F. E. Osterloh, *J. Mater. Chem. A* **2018**, 6, 5774-5781.
93. Wang, D.; Tang, J.; Zou, Z.; Ye, J. Photophysical and Photocatalytic Properties of a New Series of Visible-Light-Driven Photocatalysts  $M_3V_2O_8$  (M = Mg, Ni, Zn). *Chem. Mater.* **2005**, 17, 5177–5182.
94. Wei, S. H.; Zunger, A. Role of metal d states in II-VI semiconductors. *Phys. Rev. B* **1988**, B37, 8958.
95. Sampath, S. K.; Kanhere, D. G.; Pandey, R. Electronic structure of spinel oxides: zinc aluminate and zinc gallate. *J. Phys.: Condens. Matter* **1999**, 11, 3635.
96. Kato, H.; Kobayashi, H.; Kudo, A. Role of  $Ag^+$  in the Band Structures and Photocatalytic Properties of  $AgMO_3$  (M: Ta and Nb) with the Perovskite Structure. *J. Phys. Chem. B* **2002**, 106, 12441–12447.

Table of Contents entry:



Text to be displayed with TOC:

A quick approach to metastable oxide  $\text{Zn}_4\text{V}_2\text{O}_9$  and its photoresponse.